Scientific Study of Data Analysis

UAH

NAS8-36955 D.O. 86

FINAL REPORT

by

S. T. Wu

Submitted to

National Aeronautics and Space Administration
George C. Marshall Space Flight Center
Marshall Space Flight Center, AL 35812

PRECEDING PAGE BLANK NOT FILMED

It is known that physical conditions in the solar atmosphere are strongly controlled by solar magnetic fields. Therefore, the measurement of solar magnetic fields is essential to the understanding of the physics of the solar atmosphere. The ground-based measurements have been obtained for some time. Making solar magnetic field measurements in space would have better resolution. In this study we conducted an investigation and assessment and planning to build such a facility on board space station (or a moon-based observatory) to measure solar magnetic fields from space. This was accomplished through participation in scientific studies. Specifically the following were completed:

Dr. Rainer Kress, visited MSFC/Space Science Laboratory and UAH to discuss and gave seminar on mathematical methods related to extrapolation of solar magnetic fields March 15 - 20, 1991. These discussions led to an article "A Comparison Between Progressive Extension Method (PEM) and Iteratiave Method (IM) for Magnetic Field Extrapolations in the Solar Atmosphere" by S. T. Wu, M. t. Sun and T. Sakurai, published in Mem S.A.It., 1990, Vol. 61, No. 2, pp 477-484. (See attachment)

Dr. Petrus Martens visit UAH and MSFC/Space Science Laboratory on November 27-30 1990 to discuss the shear motion instability related to flare onset. These discussions lead to an article to be published entitled "Shear-Induced Instability and Arch Filament Eruption: A Magnetohydrodynamic (MHD) Numerical Simulation" by S. T. Wu, M. T. Song, P. C. H. Martens, and M. Dryer, Solar Physics, 134, 353-377, 1991. (See attachment)

Dr. J. P. Rozelot visited UAH and MSFC/Space Science Laboratory on November 26 - 28, 1990 to discuss the reconstruction of the solar cycle and make brief presentation on large active mirrors in aluminum, for new generation of telescopes.

These discussions and seminars provided the advancement of key concepts and technology in this planning for observations of solar magnetic fields with space qualified instrumentation.

A COMPARISON BETWEEN PROGRESSIVE EXTENSION METHOD (PEM) AND ITERATIVE METHOD (IM) FOR MAGNETIC FIELD EXTRAPOLATIONS IN THE SOLAR ATMOSPHERE

S. T. Wu and M. T. Sun
Center for Space Plasma and Aeronomic Research
and Department of Mechanical Engineering
The University of Alabama in Huntsville
Huntsville, AL 35899 USA
and
Takashi Sakurai
National Astronomical Observatory
Mataka, Tokyo, 181 Japan

ABSTRACT

In this paper we present a comparison between two numerical methods for the extrapolation of nonlinear force-free magnetic fields, viz. (i) the Iterative Method (IM) and (ii) the Progressive Extension Method (PEM). The advantages and disadvantages of these two methods are summarized and the accuracy and numerical instability are discussed. On the basis of this investigation, we claim that the two methods do resemble each other qualitatively.

I. INTRODUCTION

It is wellknown that the magnetic fields play a dominant role in all physical features which appear in the solar atmosphere; for example, the observed filamentary structures in the chromosphere seen in H_α (Martin, 1980), and coronal loops seen in UV (Cheng, et al. 1982) and X-rays (Antonucci et al. 1982; de Jager et al. 1983). All these structures in the solar atmosphere are generally considered to be aligned along the magnetic field (Zirin, 1971; Poletto, et al., 1975). Physically, these structures can be interpreted as plasma confined by the magnetic field. Hence, a detailed and quantitative analysis of these structures require a quantitative knowledge of the magnetic field in the solar atmosphere. Presently, measurements of magnetic fields are

confined to the photospheric level; therefore, in higher levels (i.e. chromosphere and corona) the magnetic field can only be obtained through numerical extrapolation using the measured photospheric magnetic field as the source surface, as demonstrated in the early work of Schmidt (1964), Altschuler and Newkirk (1969), Nakagawa and Raadu (1972). All these early extrapolation methods are restricted to the linear approximation, which physically represents current-free field (potential field) or constant current-to-magnetic field ratio (linear force free field). It has been shown that these representations are far from realistic in describing the observed features in the solar atmosphere (Schmahl et al., 1982).

In order to improve our understanding of the physical structures of the solar atmosphere it is necessary to have quantitative knowledge of the magnetic field. Therefore, a number of extraplation methods is developed to meet the demands. The mathematical model using a force free configuration on the basis for the extrapolation of photospheric vector magnetograms to obtain the coronal field has been given by Aly (1989) and Gary (1990). In particular, Gary (1990) presented an excellent summary and assessment on the present available extrapolation methods from a theoretical point of view. In this paper, a comparison between the progressive extension method (PEM) and iterative method (IM) is presented. The rationale for choosing these two extrapolation techniques for comparison is that they are based on observed photospheric level fields and have practical applications. A brief description of the theoretical background of these two techniques is presented in Section 2. Numerical results of direct comparison are included in Section 3. The discussion of advantages and disadvantages of these two techniques and their possible physical consequences are presented in section 4.

II. THEORY AND TECHNIQUES

On the assumption of magnetohydrostatic equilibrium in the solar atmosphere, the mathematical model describing such an equilibrium state may be written as

$$-\nabla p + \vec{J} \times \vec{B} - \rho \vec{g} = 0 , \tag{1}$$

where p is the hydrostatic pressure and will be represented by the equation of state,

$$p = \rho RT , \tag{2}$$

with ρ and T being the mass density and temperature respectively. The other symbols have their usual meanings; B is the magnetic field and J, the current density, is related to B by

$$\vec{J} = 7 \times \vec{B} \ . \tag{3}$$

Finally, $\vec{g}$ is the gravitational acceleration. Physically, there are three different orders of approximation to determine the magnetic field configuration. The first and second order approximations are the current free (potential) and force-free magnetic field, respectively. Within these orders of approximation the magnetic force vanishes, and the pressure force is balanced by the gravitational force which leads to the hydrostatic equilibrium in the solar atmosphere. Under these circumstances, the mathematical model for the magnetic field configuration can be represented by

$$7 \times \vec{B} = \alpha\vec{B} \ , \tag{4}$$

This expression possesses three different physical meanings, which are: (i) $\alpha = 0$, corresponds to the current free case in which the magnetic field is potential, (ii) $\alpha = $ constant, corresponds to the linear force-free magnetic field which implies a constant current-to-magnetic field ratio in a region and (iii) $\alpha = \alpha(\vec{r})$, corresponds to the nonlinear force-free field which implies a non-constant current-to-magnetic field ratio in a region.

Finally, the third order of appoximation is the magnetohydrostatic equilibrium in the solar atmosphere which is given by Eq. (1). If there is information on B and p on the source surface, it is possible to extrapolate B and p upward. Since there only are measurements of the magnetic field on the source surface (photosphere), it is not possible to extrapolate magnetohydrostatic equilibrium field-configurations at the present time.

In the meantime, we shall focus our attention on the nonlinear force-free field configuration. For the purpose of this paper, we have selected two techniques for this investigation. These two techniques are progressive extension method (PEM) (Wu et al., 1985, 1990) and iterative method (IM) (Sakurai, 1981). A brief description of these two methods is presented below:

Progressive Extension Method (PEM)

The progressive extension method is formulated as an initial-value problem (i.e., Cauchy problem) using a finite difference scheme which is similar to a Taylor expansion. A detailed description of this method is given by Wu et al. (1990). They have demonstrated the usefulness of this method, and the numerical algorithm has been verified by extrapolation of an analytical solution (Low, 1982).

A number of authors (see references in Gary, 1990) have utilized an iterative method originated by Grad and Rubin (1958) to extrapolate the nonlinear force-free magnetic field from boundary data.   For convenience, we simply choose the iterative method developed by Sakurai (1981) in this study.   His method is based the integral equation representation of Eq. (1), and the discretization is made by the technique of finite element method.   A detailed description of this technique was given by Sakurai (1981), and we shall not repeat it here.

III.   NUMERICAL RESULTS

In order to make comparison between the PEM (Progressive Extension Method) of Wu et al. (1985, 1990) and the IM (Iterative Method) of Sakurai (1981), we have chosen the vectoral magnetic field observed at Okayama Astrophysical Observatory on May 26, 1985 (Sakurai and Makita, 1986) as the boundary for extrapolation using these two methods.   The observed magnetic field vector is shown in Figure 1.

MC526C DATE: 83/5/26 TIME (JST): 10 2 13 -11 13 5
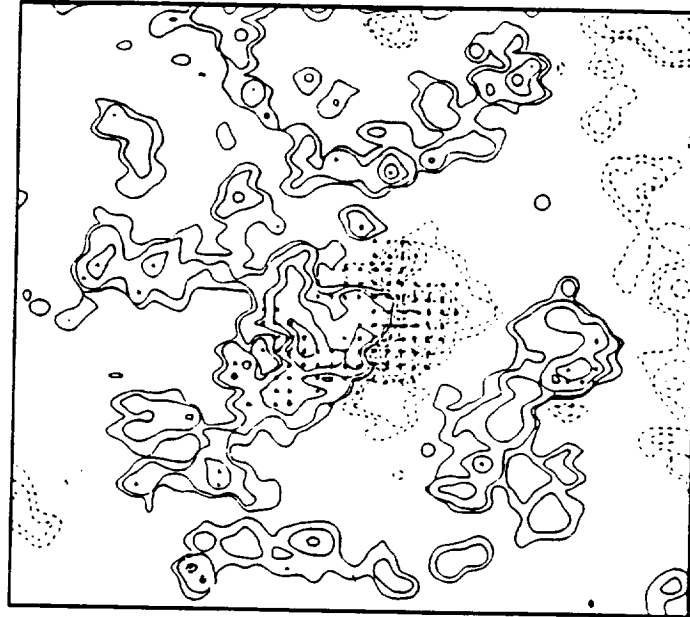OBSERVED FIELD VECTOR

Figure   1.   Magnetic   field   vector   observed   at   Okayama Astrophysical Observatory on May 26, 1983.   Solid and dotted contours show positive and negative longitudinal fields, respectively, with levels ± 10, 20, 50, 100, 200, 500 G.   Arrows indicate the transverse vector.

Using these obsc.vational data as a source surface, we obtained the nonlinear force-free field configuration by using the above mentioned two methods as shown in Figure 2, where Figure 2a is obtained by using the IM and Figure 2b by using PEM. In addition we have extrapolated the potential field configuration using PEM in comparison with the potential field given by Sakurai and Makita (1986), see Figure 3. From these results, observe that the deduced magnetic field configurations albeit not identical, in fact, qualitatively resemble each other to a large extent.

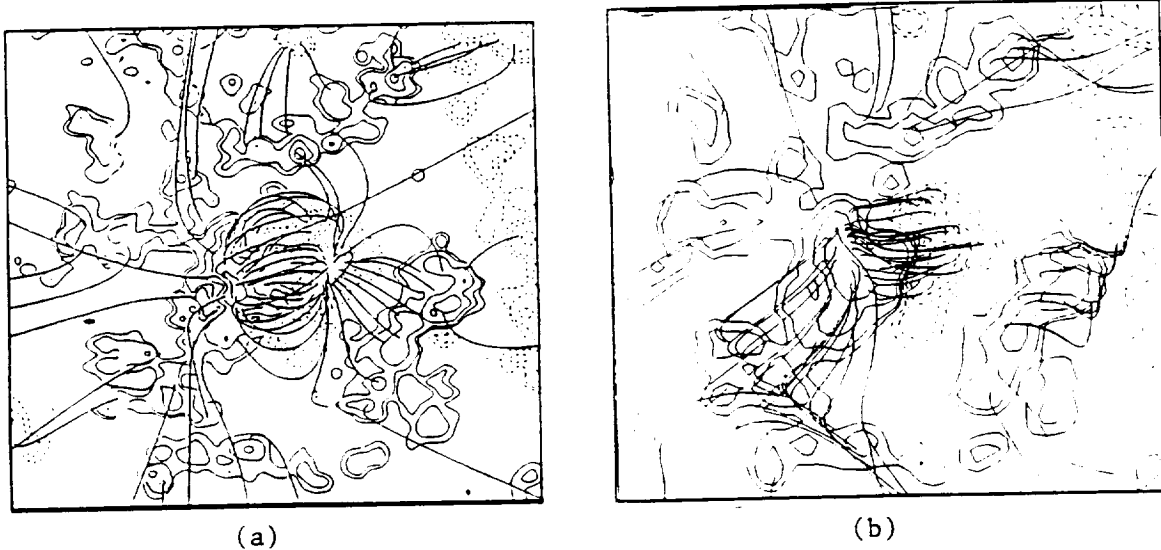(a)   (b)

Figure 2.   Nonlinear force-free field lines computed by (a) Iterative Method (IM) and (b) by Progressive Extension Method (PEM) using the data shown in Figure 1.
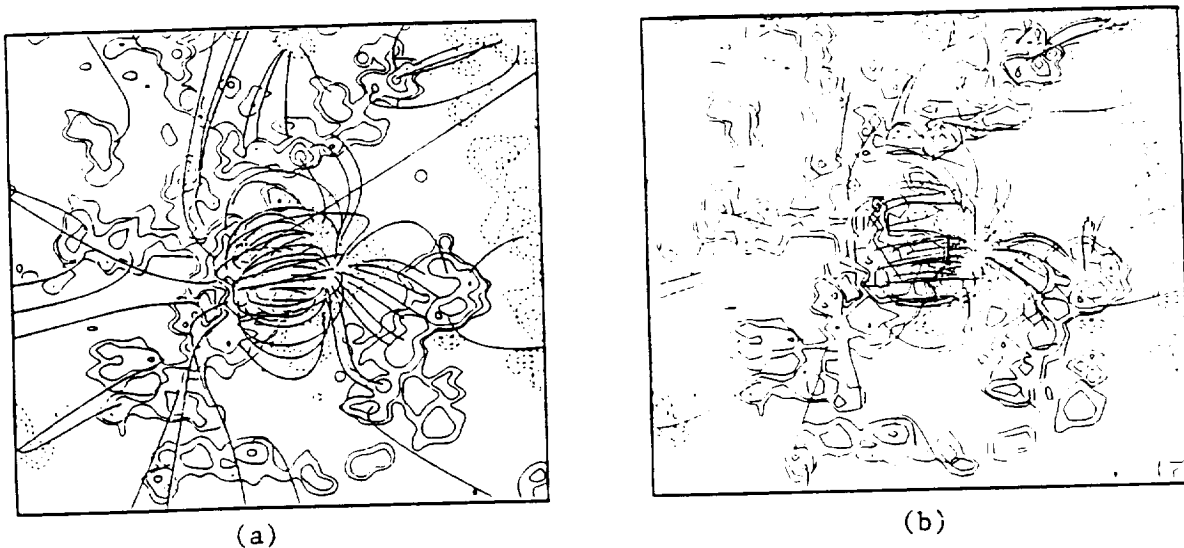

(a)   (b)

Figure 3.   (a) Potential field lines computed by IM and (b) potential field lines computed by PEM using the observation given in Figure 1.

IV. DISCUSSION

Before we analyze the causes of these differences seen in the two extrapolations we review the fundamental differences between the two methods. These differences can be summarized as follows:

1. The Iterataive Method (IM) specifies the value of α on a portion of the boundary plane (e.g. on a positive field region) and cannot assign the value of α on the whole boundary plane, since that would introduce an inconsistency in the extrapolation process. The values of α in the whole boundary plane are determined by the observed data for PEM. In this fashion, there is an electric current only along the particular field line in the IM extrapolation, while the electric current is distributed in the whole domain of calculation for the PEM extrapolation.

2. The IM type of extraplation is convergent only for small values of α. Physically, this implies that the electric current in the region of interest must be small. On the other hand, the PEM type of extrapolation does not have this limitation. However, the accuracy of the computed α-value deteriorates at the points near the neutral line (i.e. $B_z \to 0$). This may cause a misrepresentation of the magnetic field configuration. The grid size of the extrapolation is controlled by the numerical stability criteria as given by Wu et al. (1990).

3. The fact that the value of α is assigned at one of the two foot points of a particular field line in the IM while the values of α are determined on the entire boundary surface in the PEM makes it difficult to match and compare the field lines for these two different methods.

On the basis of these differences of extrapolation procedures, we may understand why the magnetic field configurations obtained from the same data with these two methods are not identical. For example, Figure 2, shows some differences in magnetic field-line configurations, but the lines connecting different regions of polarities are quite similar. Note that for two regions of opposite polarities near the right center, the PEM extrapolation doesn't show any connection by field lines, while the IM type extrapolation does. However this is due simply to the fact that the field lines in this region are very low and short, and cannot be discerned in this drawing. Plots of the front view of Figure 2b, clearly indicate that the regions are connected by field lines (marked by A) as shown in Figure 4.
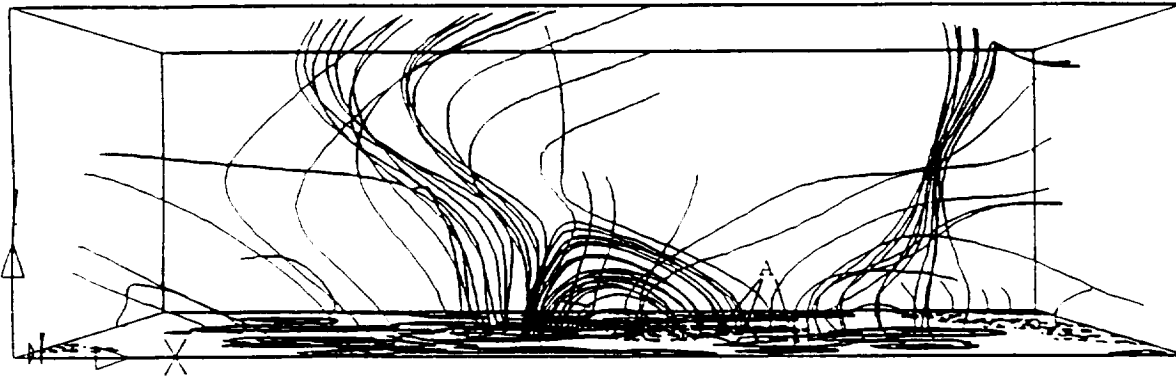
Figure 4.   The front view of the nonlinear force-free field
computed by PEM using the observtion given in Figure
1.   It should be noted that the field lines near the
top are not accurate due to numerical procedure as
discussed by Wu et al. (1990).

We further notice that the configuration of the field lines
obtained by IM extrapolation is very similar to a potential field
line configuration.   This is because the IM requires that the
value of α be small (i.e. slightly deviating from potential).
On the other hand, the PEM extrapolation does not have this
limitation.   It is understood that the degree of deviation from
a potential field depends on the value of α, that is the strength
of the local electric current.   Therefore, the configuration of
magnetic field lines is affected.

In summary, we conclude:
(i) Both methods do produce qualitatively similar results.
(ii) The accuracy of PEM has been verified by an analytical
solution (Wu et al. 1990); verification of IM is still
needed.
(iii) There are limitations on the value of α for IM, but not
for PEM.
(iv) The accuracy for PEM deteriorates when the height of
extrapolation exceeds one third the horizontal length,
because of the propagation of the accummulated
numerical errors at each level (Wu et al. 1990).

ACKNOWLEDGEMENT

REFERENCES

Altschuler, M. D. and Newkirk, G., Jr.: 1969, Solar Physics, 9, 131.

Aly, J. J.: 1989, Solar Physics, 120, 19.

Antonucci, E, Gabriel, A. H., Acton, L. W., Culhand, J. L. Doyle, J. G., Liebacher, J. W., Machado, M. E., Orwig, L. E. and Rapley, C. G.: 1982, Solar Physics, 73, 107.

Cheng, C. C, Bruner, E. C., Tandberg-Hanssen, E., Woodgate, B. E., Shine, R. A., Kenny, P. JU., Henze, W., and Poletto, G.: 1982, Ap. J., 253, 353.

deJager, C., Machado, M. E., Schadee, A., Strong, K. T., Svestka, Z., Woodgate, B. E. and van Tend, W.: 1983, Solar Physics, 84, 205.

Gary, G. A.: Mem. della Soc. Astr. Italiana, this issue.

Grad, H.and Rubin, H.: 1958, in Proc. 2nd International Conference Peaceful Uses of Atomic Energy, Vol. 13, Geneva, United Nations, p. 190.

Low, B., C.: 1982, Solar Physics, 77, 43.

Martin, S. F.: 1980, Solar Physics, 68, 217.

Nakagawa, Y. and Raadu, M. A.: 1972, Solar Physics, 25, 127

Poletto, G., Vaiana, G. S., Zombeck, M. V., Krieger, A. S. and Timothy, A. F.: 1975, Solar Physics, 44, 83.

Sakurai, T.: 1981, Solar Physics, 69, 343.

Sakurai, T. and Makita, M.: 1986, in Y. Osaki (ed.) Hydrodynamics and Magnetohydrodynamic Problems in the Sun and Stars, University of Tokyo, 53.

Schmal, E., Kundu, M. R., Strong, K. T., Bentley, R. D., Smith, J. B., Jr., and Krall, K. R.: 1982, Solar Physics, 80, 233.

Schmidt, H. U.: 1964 in W. N. Hess (ed.), Physics of Solar Flares, NASA SP-50, 107.

Wu, S. T., Chang, H. M. and Hagyard, M. J.: 1985, NASA CP-2347, 17.

Wu, S. T., Sun, M. T., Chang, H. M., Hagyard, M. J., and Gary, G. A.: 1990, Astrophys. J. (in press).

SHEAR-INDUCED INSTABILITY AND ARCH FILAMENT ERUPTION: A MAGNETOHYDRODYNAMIC (MHD) NUMERICAL SIMULATION

S. T. WU and M. T. SONG*

Department of Mechanical Engineering and Center for Space Plasma and Aeronomic Research. The University of Alabama in Huntsville. Huntsville. AL 35899. U.S.A.

P. C. H. MARTENS

Harvard–Smithsonian Center for Astrophysics. Cambridge. MA 02138. U.S.A.

and

Lockheed Palo Alto Research Laboratories. Palo Alto. CA 94304. U.S.A.

and

M. DRYER

Space Environment Laboratory. National Oceanic and Atmospheric Administration. Boulder. CO 80303. U.S.A.

Abstract. We investigate, via a two-dimensional (nonplanar) MHD simulation, a situation wherein a bipolar magnetic field embedded in a stratified solar atmosphere (i.e., arch-filament-like structure) undergoes symmetrical shear motion at the footpoints. It was found that the vertical plasma flow velocities grow exponentially leading to a new type of global MHD-instability that could be characterized as a 'Dynamic Shearing Instability', with a growth rate of about $\sqrt{8}\,\overline{V}_A a$, where $\overline{V}_A$ is the average Alfvén speed and a^{-1} is the characteristic length scale. The growth rate grows almost linearly until it reaches the same order of magnitude as the Alfvén speed. Then a nonlinear MHD instability occurs beyond this point. This simulation indicates the following physical consequences: the central loops are pinched by opposing Lorentz forces. and the outer closed loops stretch upward with the vertically-rising mass flow. This instability may apply to arch filament eruptions (AFE) and coronal mass ejections (CMEs).

To illustrate the nonlinear dynamical shearing instability, a numerical example is given for three different values of the plasma beta that span several orders of magnitude. The numerical results were analyzed using a linearized asymptotic approach in which an analytical approximate solution for velocity growth is presented. Finally, this theoretical model is applied to describe the arch filament eruption as well as CMEs.

1. Introduction

More than a quarter century ago, Gold and Hoyle (1960) suggested that horizontal photospheric motion can move the footpoints of magnetic field lines and twist the flux tubes because of the highly electric conducting plasma at the photospheric levels. A number of investigators (Tanaka and Nakagawa, 1973; Low and Nakagawa. 1975: Low. 1977: Klimchuk. Sturrock, and Yang, 1988: Klimchuk and Sturrock. 1989) studied the evolution of force-free fields and its role in energy storage (build-up) for solar flares.

* Permanent address: Purple Mountain Observatory, Nanjing, China.

All of these studies were limited to the case of magnetostatics: self-consistent dynamical effects were ignored. Recently, Wu, Hu, and Nakagawa (1983), Wu, Hu, and Krall (1984), and Wu et al. (1986) presented a self-consistent MHD model for the purpose of examining flare energy build-up and wave-mass interactions due to shear and converging-diverging motions at the photospheric level. More recently, Mikic, Barnes, and Schnack (1988) and Biskamp and Welter (1989) have presented numerical results on the dynamical evolution of a magnetic arcade type due to shear motion. However, their models are restricted to symmetric boundary conditions, while in this study self-consistent boundary conditions were used (see, for example, Wu and Wang, 1987; Nakagawa, Hu, and Wu, 1987).

In this paper, we use the time-dependent MHD simulation model devised by Wu, Hu, and Nakagawa (1983) to reveal a nonlinear solution for the evolution of the magnetic field configuration driven by shear motion. In this solution, we find that the plasma velocity in the vertical plane perpendicular to the shear, grows exponentially in a process which can be analytically described by a linear MHD instability. This upward velocity steadily increases until it reaches the average Alfvén speed. At later times, a nonlinear instability sets in. A field line pinch occurs in the lower shear region in the numerical results. At the same time, mass and field line expulsion appears in higher parts of the region and the closed field tends to open locally. We suggest that these new effects (i.e., mushroom cloud-like flow, pinch, and expulsion) can explain the formation of current sheets, the opening of a closed bipolar field, and the ability of particle streams to escape from the solar surface. Specifically, we suggest that this model applies to the eruption of arch filament systems (AFEs) and their relation to non-flare-associated coronal mass ejections (CMEs). The mathematical description of the model and numerical results are given in Section 2. A general physical interpretation of these results is presented in Section 3. An application of this model to specific coronal phenomena is given in Section 4, and the concluding remarks are presented in Section 5.

2. Numerical Simulation

In order to illustate how shear-induced non-equilibrium occurs, we use a theoretical model in which a two-dimensional bipolar field undergoes a steady shear velocity at the footpoints of its magnetic loops. The shearing motion is sketched in Figure 1(a), and the initial bipolar field is shown explicitly in Figure 1(b).

First, we perform a simulation of the dynamic response of the bipolar field to the shear. Then we use an analytical method to interpret the simulation results. The simulation model is based on a two-dimensional, time-dependent, MHD model (Wu, Hu, and Nakagawa, 1983; Hu and Wu, 1984) with an improved FICE (Full-Implicit-Continuous-Eulerian) numerical scheme (Wu and Wang, 1987). Symmetrical side boundary conditions have been replaced with non-reflecting boundary conditions. This implies that the physical phenomena are determined by the solution at a specific time and are not determined by the specified boundary conditions as in the case studied by Mikic, Barnes, and Schnack (1988). The physical conditions on these
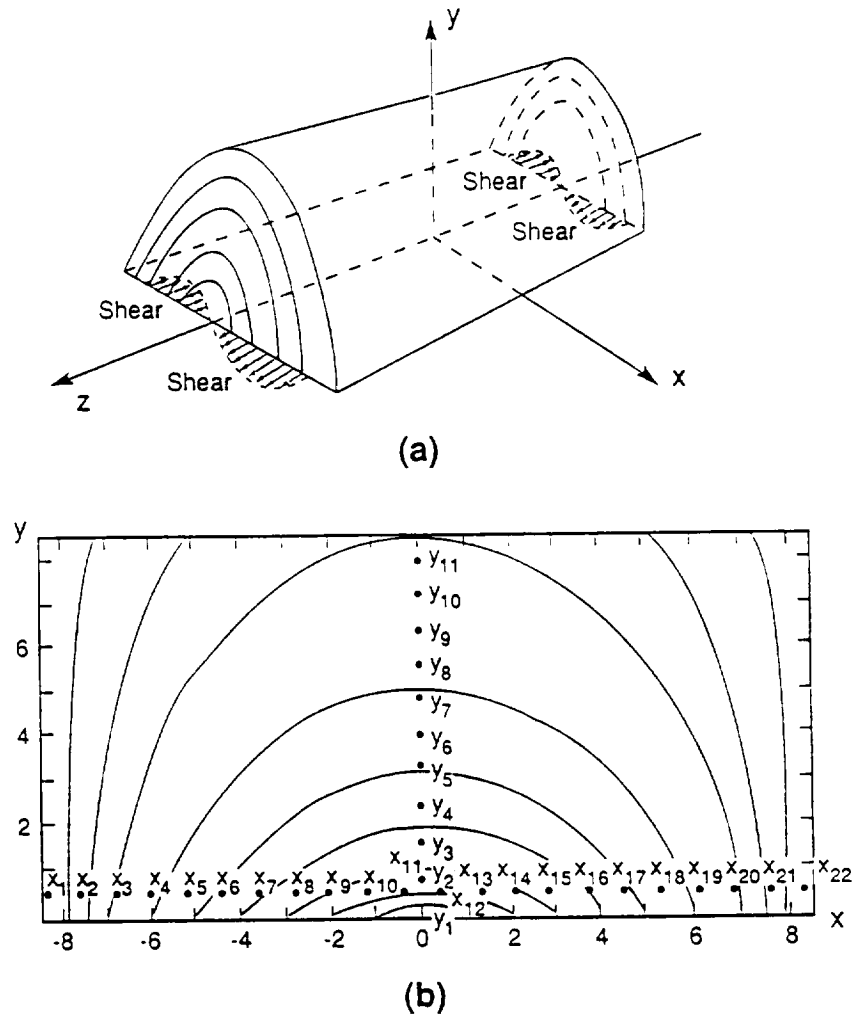
Fig. 1. (a) Sketch of a two-dimensional bipolar magnetic field that is subjected to a footpoint shearing motion as indicated by the arrows. (b) Explicit bipolar magnetic topology prior to the shearing motion (see Equation (1)). The photospheric boundary extends to $|x| = 8.4 \times 10^3$ km in both directions from the origin. The vertical extent into the corona is to $y = 8 \times 10^3$ km. The positions $y = y_1, y_2, \ldots, y_{10}$ indicate the vertical levels at which horizontal surveys will be shown of various physical quantities during the shearing motion at the footpoints.

two side boundaries are determined mathematically through compatibility relations that are given in detail by Wu and Wang (1987). Thus, the computation domain (i.e., $|x| \leq 8.4 \times 10^3$ km, $0 \leq y \leq 8 \times 10^3$ km) consists of three free non-reflecting boundaries (i.e., top and sides), while the bottom boundary ($y = 0$) is treated with the method of projected characteristics (Nakagawa, Hu, and Wu, 1987; Hu and Wu, 1984). The basic equations for this model are the time-dependent MHD equations with infinite conductivity, no viscosity and symmetry in one direction (Wu, Hu, and Nakagawa. 1983). Solar gravity, plasma pressure gradients, and compressibility are explicitly considered. None of these characteristics were considered in the work of Mikic, Barnes. and Schnack (1988), and Biskamp and Welter (1989) have only considered compressibility in a special way.

The initial conditions are (see Figure 1(b)):

$$\rho_0 = \rho_c \exp\left(-\frac{gy}{RT_c}\right), \quad T_0 = T_c, \quad v_x, v_y, v_z = 0.$$

$$B_{x0} = B_0\left[\cos(ax)\right]e^{-ay}, \quad B_{y0} = -B_0\left[\sin(ax)\right]e^{-ay}, \quad B_{z0} = 0. \tag{1}$$

$$a = \pi/2x_0, \quad x_0 = 8.4 \times 10^3 \text{ km}, \quad g = 2.71 \times 10^4 \text{ cm s}^{-2}.$$

The plasma parameters are taken to be $\rho_c = 1.67 \times 10^{-12}$ g cm^{-3} and $T_c = 10^5$ K. The scale height ($b^{-1} = RT_c/g \sim 6.1 \times 10^3$ km) and $a^{-1} \sim 6.3 \times 10^3$ km are the same order of magnitude. These parameters are representative for solar conditions at the higher chromosphere and lower corona. The computation grid points are:

$$x_i = -8.4 \times 10^3 + (i - 1)\Delta x, \quad i = 1, 2, \ldots, 22.$$

$$y_j = (j - 1)\Delta y, \quad j = 1, 2, \ldots, 11,$$

$$\Delta x = \Delta y = 8 \times 10^2 \text{ km} \sim 1 \text{ arc sec}.$$

The non-reflecting boundary conditions, as noted above, are used for the top ($y = y_{11}$), left-hand side ($x = x_1$), and right-hand side ($x = x_{22}$). The conditions at the bottom boundary ($y = y_1$) are taken as follows:

$$\rho = \rho_c, \quad T = T_c, \quad B_y = B_{y0}, \quad v_x = 0, \quad \text{but} \quad v_y, v_z \neq 0.$$

$$v_z = \begin{cases} w_c \sin(ax) & \text{if } |x| \le 5.2 \times 10^3 \text{ km}, \\[2mm] \dfrac{(6.8 \times 10^3 - x_i)}{1.6 \times 10^3} w_c (\text{sgn } x) \sin(5.2 \times 10^3 a) & \\ \quad \text{if } 5.2 \times 10^3 < |x| \le 6.8 \times 10^3 \text{ km}, \\[2mm] 0 & \text{if } 6.8 \times 10^3 < |x| < 8 \times 10^3 \text{ km}. \end{cases} \tag{2}$$

The other physical quantities (ρ, T, v_y, B_x, B_z) are computed by means of the compatibility equations for the non-reflecting boundary condition which assures the consistency of the numerical computation.

In order to understand the general physical behaviour of the nonlinear solution from the mathematical model, we have performed three numerical experiments. These three cases use combinations of magnetic field intensity and magnitudes of the shear velocity. The results for these three cases are described as follows.

2.1. LARGE PLASMA BETA ($\beta_0 \simeq 154$)

In this numerical experiment, we choose the initial plasma beta (β_0) to be 154 where β_0 is defined as $\beta_0 = p_0/(B_0^2/8\pi)$ with p_0 and B_0 being the plasma pressure and magnetic field strength at the lower boundary (i.e., $y = y_1$). This is not a physically realistic case for a solar active region; but it does provide a basis for comparison with the other cases. This case corresponds to a local, exceedingly low, magnetic field strength of

2.12 G at the origin, $x = y = 0$, as shown in Figure 1(b). The shear velocity, w_0, was taken to be 5 km s^{-1}. Figure 2 shows the evolution of the magnetic field lines due to the shear motion at $200\,s \le t \le 3200\,s$. It is useful to examine the evolutionary behaviour at various Alfvén times (defined as $\tau_A = [\Delta y$ (or $\Delta x)]/V_A \simeq 1700\,s$ where
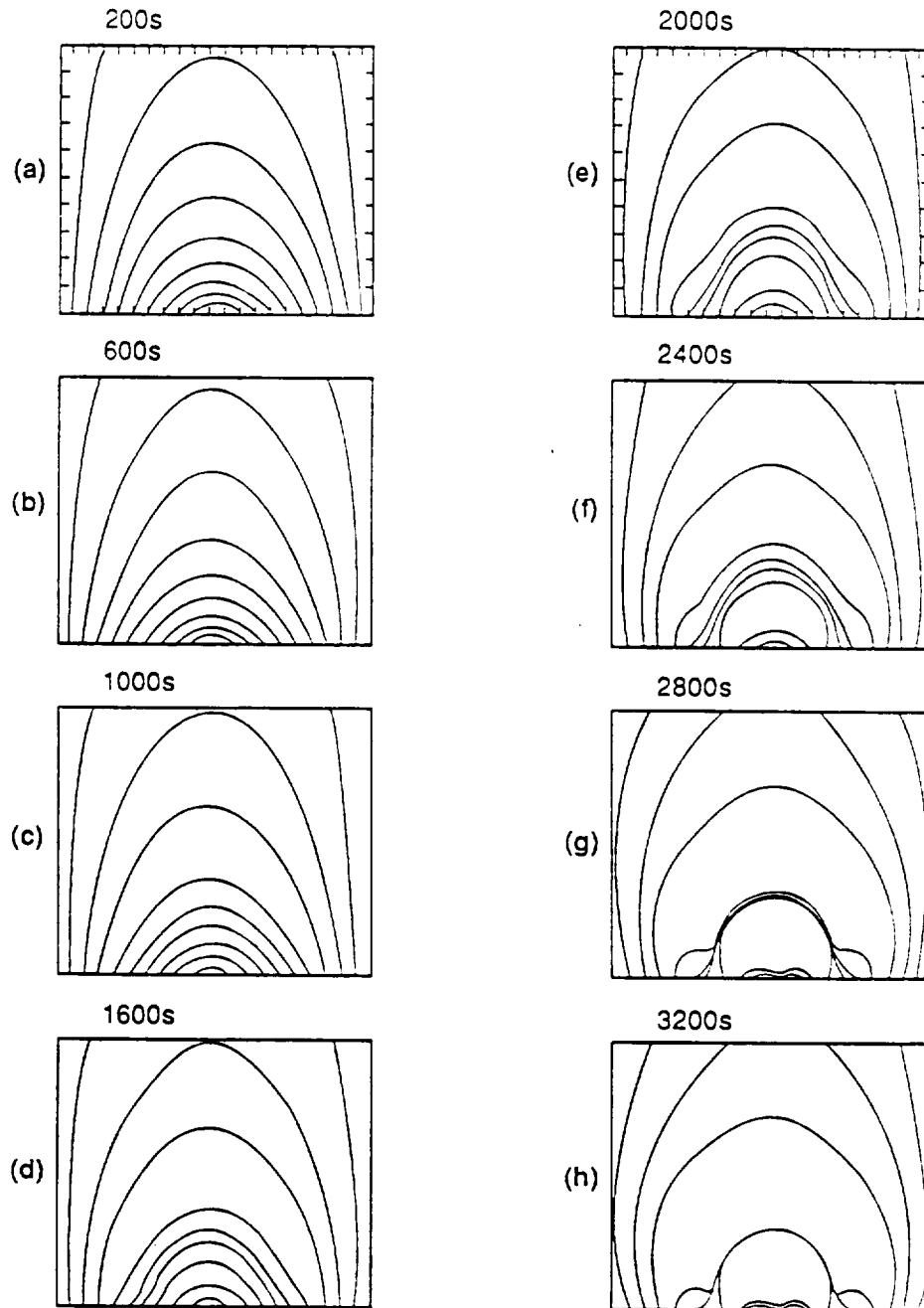
$\beta. \sim 15\,4,\ \tau_a \sim 1700s$

Fig. 2.   Magnetic field line evolution as a function of time during induced footpoint shearing motion for case (i): $\beta_0 = 154$ and the Alfvén time, $\tau_A = 1700\,s$. The horizontal axis represents the distance from $x_1 \ldots x_{22}$ as shown in Figure 1(b).

$V_A = B_0/\sqrt{4\pi\rho_0} = 4.6$ km s^{-1}). During the early stages of evolution (that is, within the first Alfvén time), the magnetic field lines rise together in an orderly fashion in response to the shearing motion. This behaviour is also presented in the analytical solution of Low (1981) and the force-free numerical solutions of Klimchuk and Sturrock (1989) although they do not consider dynamics and gravitational effects. After the first Alfvén time period, the evolutionary behaviour of the field lines becomes more complicated. Nonlinear interactions take place between the shear-induced mass motion, magnetic field and gravity with the result that in some regions the field lines are bunched together to form a current sheet (see Figures 2(g) and 2(h)). Further understanding of these phenomena is provided by the representation of the shear induced mass motion as shown by the vectorial velocity field in Figure 3. Notice that the inclusion of magnetohydrodynamic effects, in contrast to the kinematic study of Low (1981), causes upward mass motion in addition to the up-lifting of the magnetic field lines because the plasma has to move with the field lines under the conditions of infinite conductivity as manifested by the upward component of Lorentz force. Note, however, that some of the uplifted plasma (in the region displaced from the origin) slows down under the action of gravity, reverses direction, and falls back to the surface. Most of the motion, however, is upward. These upward mass motions are also found by Mikic, Barnes, and Schnack (1988) and Biskamp and Welter (1989). However, these workers did not include compressibility, pressure gradient, and gravitation as noted above. The present study, which does so explicitly, demonstrates a different evolution in the later stages.

This induced upward motion can be explained via our governing equations. When we introduce the shear motion (v_z), an axial field component, B_z, will be induced through the induction equation. The additional magnetic field will cause an additional magnetic pressure gradient in the momentum equation. This additional pressure gradient induces both the horizontal (v_x) and upward (v_y) motions as shown in Figure 3. Subsequently, the mass motion interacts with both the magnetic field and gravity. Closer to the surface, the combined effect is dominated by gravity, and the result is the cluster of magnetic field lines in which a current sheet is formed as shown in Figures 2(g) and 2(h) at nearly twice the Alfvén time.

Figure 4 shows the plasma properties (i.e., density temperature, and pressure enhancement in terms of percentage change from the initial values at each level) at the end of this simulation ($t = 3600$ s; more than $2\tau_A$). These properties are shown at various heights (y_1, y_2, y_4, y_6, and y_{10}, as shown in Figure 1(b)) as a function of horizontal distance. These results also help to explain the magnetic field line distribution. That is, the high density magnetic field region shown in Figures 2(g) and 2(h) within the mid-horizontal range (at the altitudes: y_2, y_4) corresponds to the increase of plasma density by 20% (i.e., $\Delta\rho/\bar{\rho} \sim 0.2$), temperature decrease of 20% (i.e., $\Delta T/\bar{T} \sim -0.2$), and magnetic field strength ($\Delta B/B_0$) increase by a factor of 3. These properties are similar to those for a current sheet. With these properties in mind, let us now turn our attention to the plasma flow patterns as shown in Figure 3. The plasma flow rises initially above the zone of maximum shear velocity. At later times (say, from 1000 to 2000 s), the plasma flow moves toward the central region in a pattern reminiscent of a mushroom

200s

(a)

2000s

(e)

600s

(b)

2400s

(f)

1000s

(c)

2800s

(g)

1600s

(d)

3200s

(h)

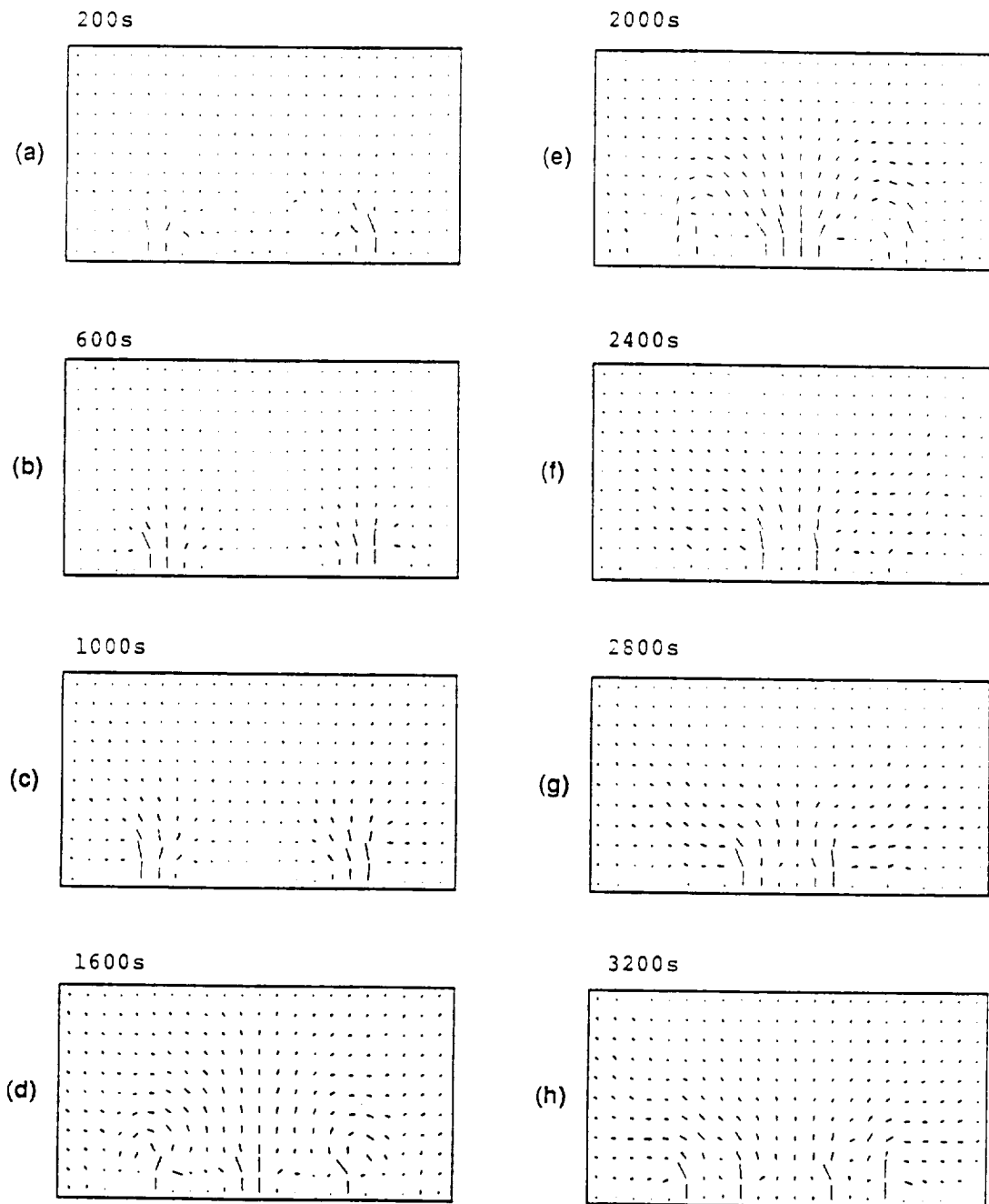Fig. 3.   Vectorial velocity field as a function of time during induced footpoint shearing motion for case (i):
$\beta_0 = 154$; $\tau_A = 1700$ s.

cloud. In the later stages as shown in Figures 3(g) and 3(h), the significant plasma motion is again concentrated in the neighbourhood of the sheared region. This is also the region where the magnetic field lines have been clustered as seen in Figures 2(g) and 2(h).
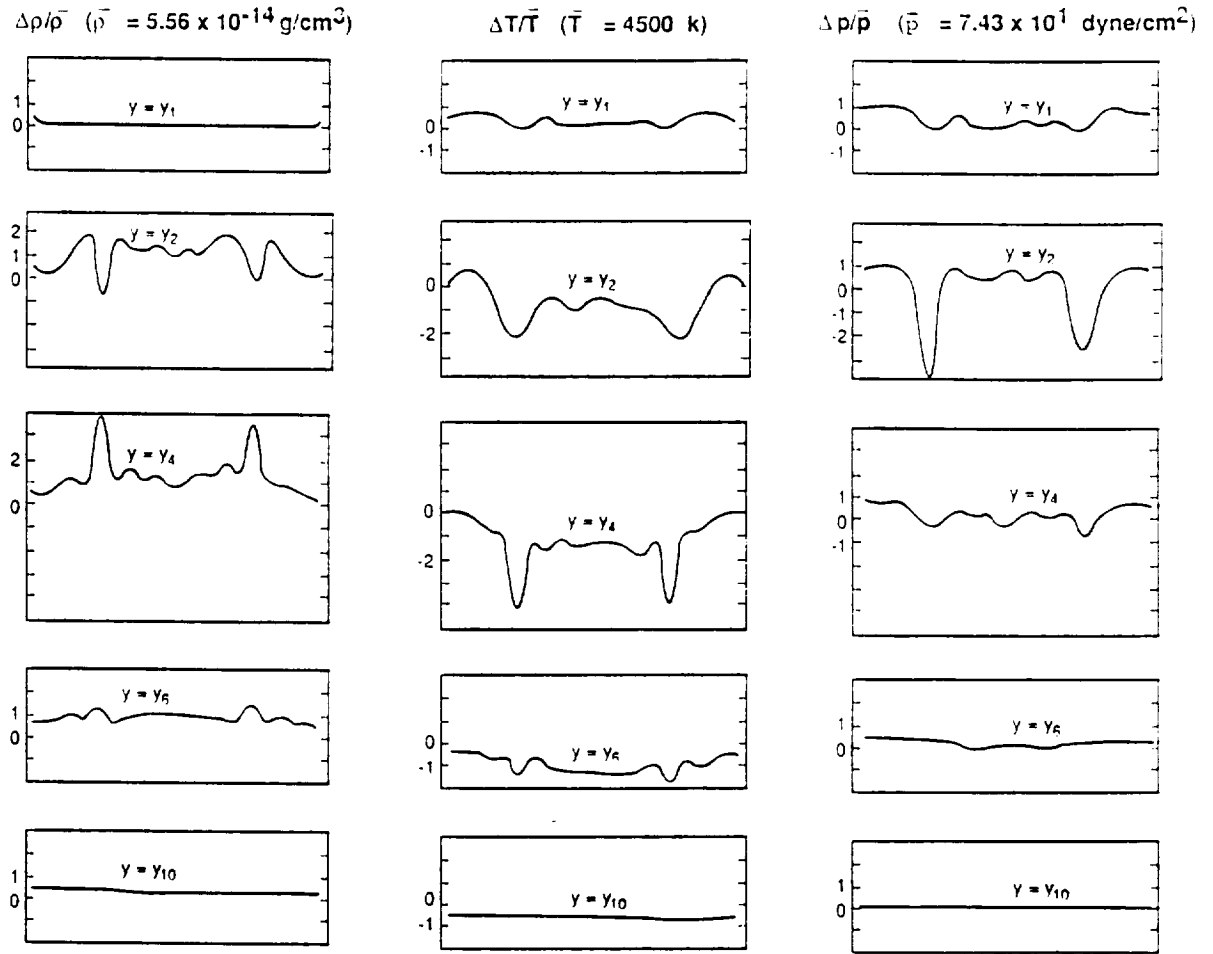
Fig. 4.   Changes (relative to the initial local values) of density ($\Delta\rho = \rho - \rho_0(y)$), temperature ($\Delta T = T - T_0$), and pressure ($\Delta p = p - p_0(y)$) normalized by a proper value as shown at the end of the simulation (case (i): $\beta_0 = 154$), $t = 3600$ s which is more than two Alfvén time periods. The distributions are plotted along the entire horizontal scale of the domain and at various levels: y_1, y_2, y_4, y_6, and y_{10} as shown in Figure 1(b). All the values are normalized by a reference quantity as indicated.

2.2. INTERMEDIATE PLASMA BETA (i.e., $\beta_0 = 1.54$)

In this case, our simulation is performed with an initially modest magnetic field strength ($B_0 = 21.3$ G) and with a shear velocity (w_c) of 15 km s^{-1} and $V_A \sim 46.5$ km s^{-1}. The qualitative behaviour of the evolution of the vectorial fields (i.e., magnetic and velocity fields) and plasma parameters (i.e., density, temperature, and pressure) are similar to case (i). Therefore, we shall not repeat a full presentation. Nevertheless, there are some interesting features that appear in the evolutionary results of the magnetic and velocity fields as shown in Figure 5.

The most pronounced result is the induced velocity distribution shown on the right side panels of Figure 5. The high velocity of the ascending movement in the central region is especially notable. As a result, the closed bipolar field tends to be opened up. We attribute this to the force created by the ascending movement of mass motion initiated by the shear prescribed at the lower boundary. The highest velocity attained by the mushroom cloud-like ascending mass motion is about 25 km s^{-1} at $t = 700$ s

$$\beta_o = 1.54$$

Magnetic Field Line   Velocity

(a)   (d)

Time = 100 s

(b)   (e)
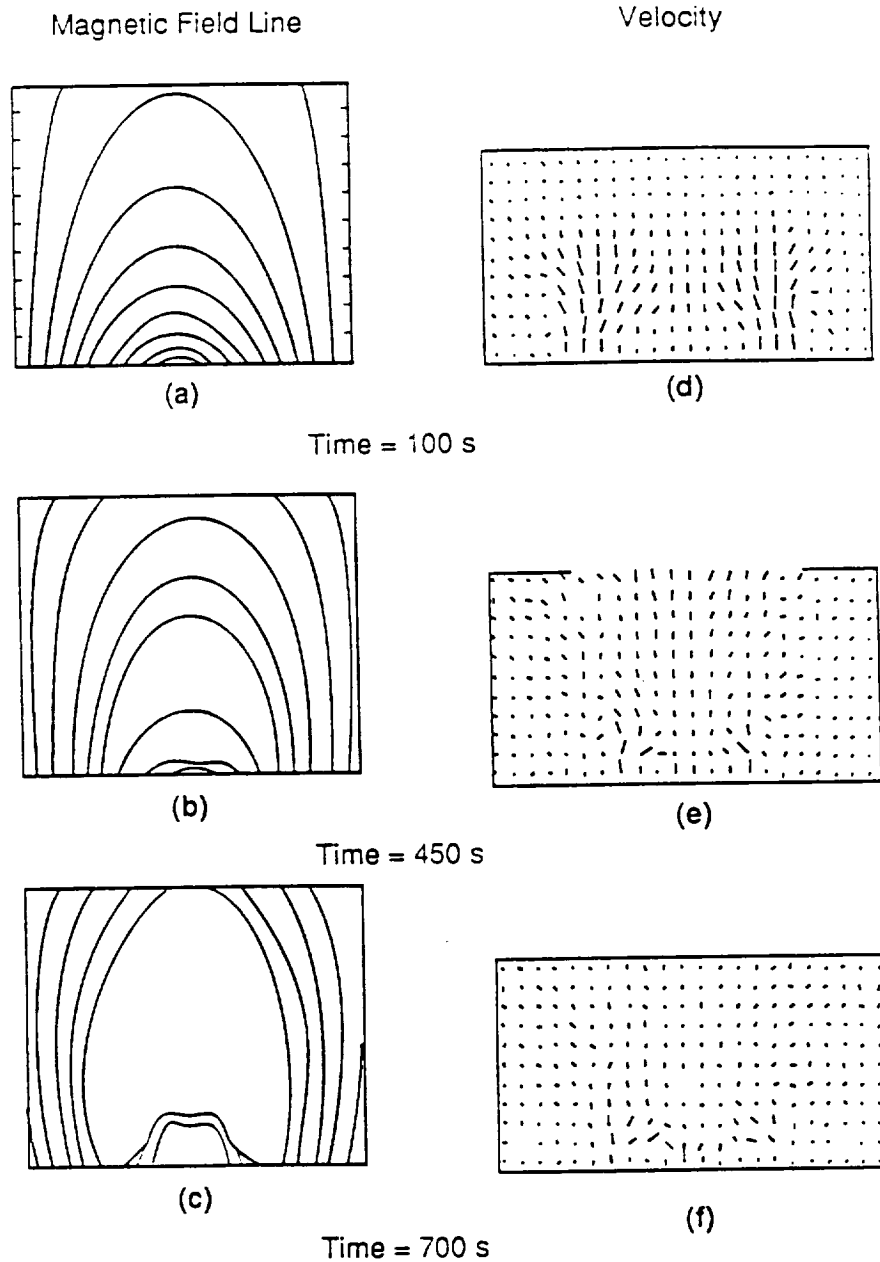
Time = 450 s

(c)

(f)

Time = 700 s

Fig. 5.   Evolution of magnetic field lines and vectorial velocity fields at various times for case (ii): $\beta_0 = 1.54$. The characteristic Alfvén time for this case is $\tau_A = 174$ s.

(i.e., ~ 4 Alfvén times) after introduction of the shear motion. The corresponding plasma parameters can be summarized as follows: the density decreases by about 50% at the legs of the intermediate loops marked by the footpoints x_4, x_5, and x_6 as labeled in Figure 1(b). Again, the pinch effects discussed for case (i) occur and a current sheet is formed where the density increases by 25%; the temperature decreases by 30%; and the field strength increases by a factor of 2.

2.3. Low plasma beta (i.e., $\beta_0 = 0.06$)

In this case the initial magnetic field strength is increased to a more realistic value of 106.3 G $w_c = 15$ km s^{-1} and $V_A = 232$ km s^{-1} without changing the other plasma parameters. The initial plasma beta is equal to 0.06 which is 250 times smaller than case (ii) and 2500 times smaller than case (i). Again, the evolution of the magnetic field and velocity field exhibits patterns similar to those of cases (i) and (ii). Figure 6 shows the evolution of the magnetic field and the velocity vector field for this case. The maximum upward velocity is a factor of 4 higher than for case (ii) and a factor of 40

$\beta_0 = 0.06$

Magnetic Field Line   Velocity

Time = 75 s

(a)   (d)

Time = 175 s

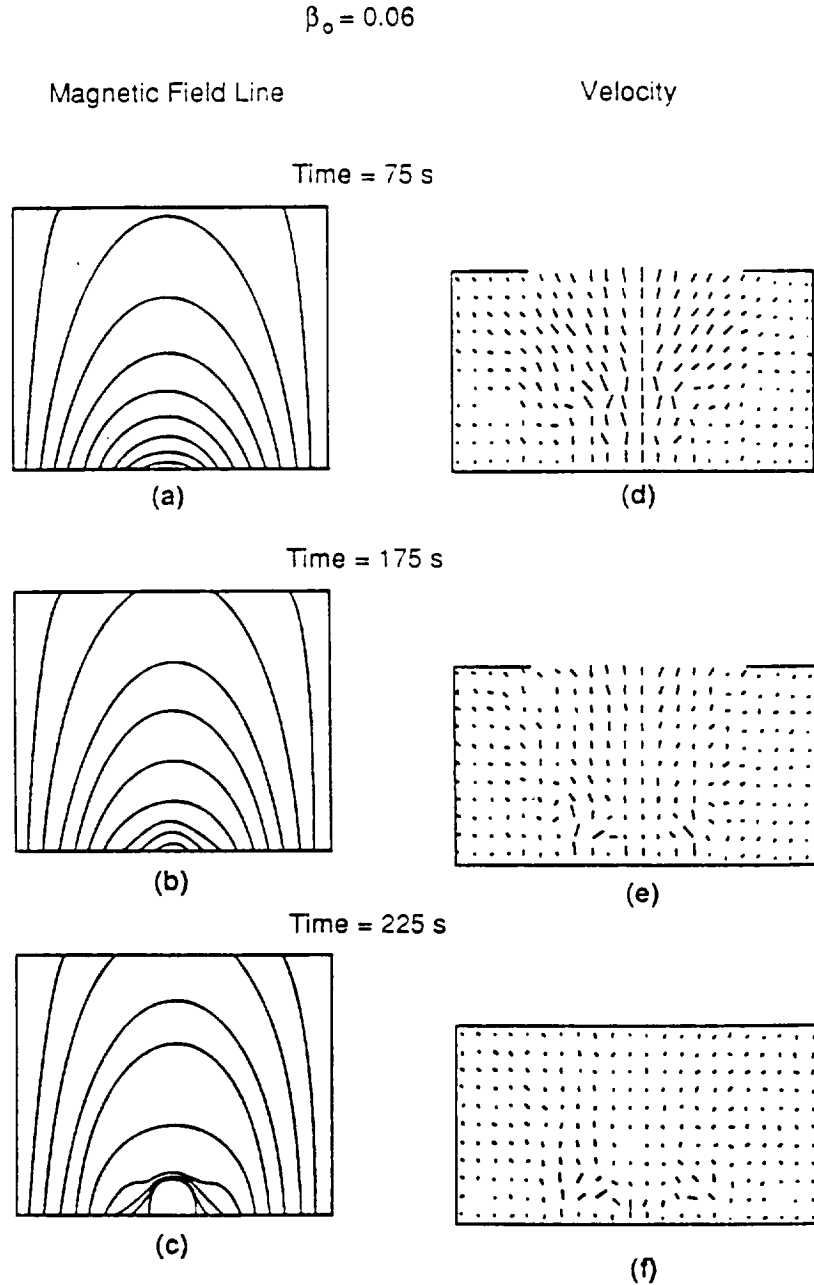(b)   (e)

Time = 225 s

(c)

(f)

Fig. 6.   Evolution of magnetic field lines and vectorial velocity fields at various times for case (iii): $\beta_0 = 0.06$. The characteristic Alfvén time for this case is $\tau_A = 35$ s.

higher than for case (i). We note that the time required to reach the maximum velocity is much shorter than in the other two cases.

In order to examine this phenomenon further. we plotted in Figure 7 the planar maximum absolute velocity (i.e.. $(v_x^2 + v_y^2)_{max}^{1/2}$) in the neighbourhood of the apex of the arcade as a function of time for the three different cases. We choose to plot this parameter instead of the upward velocity, v_y, because the representative parameter $[v_x^2 + v_y^2]^{1/2}$ is related to our analytical analysis that is discussed later (and in the Appendix). Actually, the numerical results show that the horizontal velocity, v_x, is only 25% of the vertical velocity, v_y. First, we point out the change of scales that was required for the three cases (i), (ii), and (iii). Second, we direct attention to the common features: an approximately linear initial phase followed by a smooth transition to an explosive upward mass motion. The latter phenomenon is representative of the upward regions as discussed earlier.
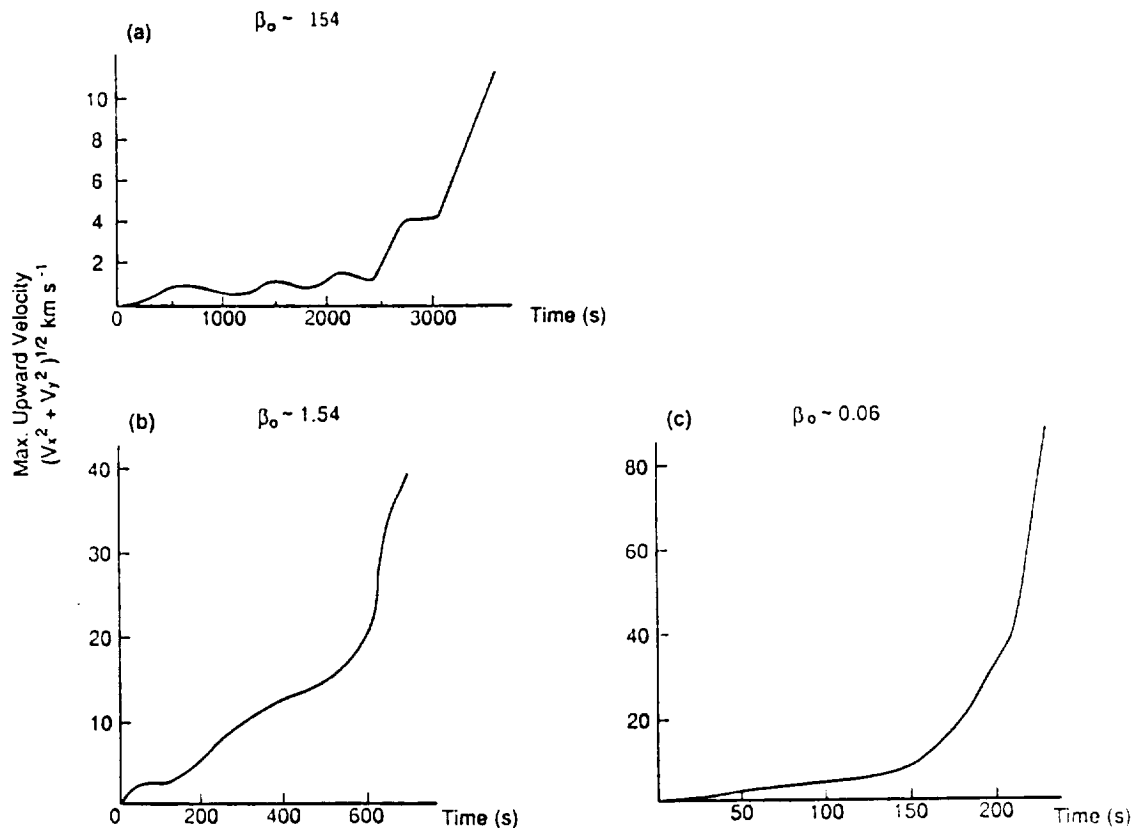
Fig. 7. Maximum vectorial velocity that is representative of the upward vertical mass motion for cases (i). (ii), and (iii). Note the change of scales. The representative Alfvén times for the three cases (β_0 = 154. 1.54. and 0.06. respectively) are τ_A = 1700 s, 174 s. and 35 s.

It is interesting to relate these results to the magnetic field evolution. For example. we direct attention to Figures 2. 5, and 6 where. in the early stages of the evolution. the change of field lines is regular with a slowly ascending movement. This upward motion is also present in the force-free analyses of Low (1981) and Klimchuk and Sturrock (1989), and the numerical incompressible simulations of Mikic, Barnes. and Schnack

(1988), and Biskamp and Welter (1989). However, the change of field lines in the present case becomes quite irregular in the later stages of the evolution. From Figures 2, 5, and 6, we notice that the lower field lines are pinched together and the upper field lines tend to open up when the maximum planar velocity exceeds the Alfvén speed. The Alfvén speed for these three cases is 4.67 km s^{-1}, 46.7 km s^{-1}, and 232 km s^{-1}, respectively. The maximum footpoint shear motion, v_z, is slow compared to the Alfvén velocity in the latter two cases but fast compared with resistive diffusion in all three cases. Thus a sequence of essentially quasi-static, force-free states with frozen-in magnetic fields is found in the early stages, which ends when the magnitude of planar maximum velocity exceeds the Alfvén speed, and the system becomes unstable. We claim that this is a shear-induced instability that could not be found in the earlier numerical simulations that omitted compressibility, pressure gradient, gravity, and the different treatment of boundary conditions. We shall return to this point later for further discussion utilizing analytical results.

3. Further Interpretation of the Simulation Results

From these simulation results, we have found that the buoyancy force leads to a mushroom cloud-like ascending movement that pushes the closed magnetic field upward. In order to understand this result further, we supplement our numerical simulation with an approximate analytical solution:

3.1. Creation of mushroom cloud-like ascending motion

From the numerical simulation of all three cases, we observe that the shear-induced mushroom cloud-like ascending movement can be ascribed to the out-of-plane component of the magnetic field, B_z. This component gives an upward magnetic pressure gradient (i.e., $\nabla(B_z^2/8\pi)$) which causes the ascending movement of magnetic field and corresponding plasma flows. On the other hand, we notice that no B_z component is generated near the origin ($x = 0$, $y = 0$) due to shear. This leads to a downward force, such that we observe the field lines being squeezed together to form a current sheet as shown in Figures 2, 5, and 6. This point can be illustrated further by using a linear approximation. The justification for the use of linear theory is seen from the numerical results that show that the initial stage of the shear-induced motion behaves regularly as shown in Figures 2, 3, 5, and 6.

A closed form linearized solution for the induced field component B_z is the following (for the derivation, see the Appendix):

$$\frac{B_z}{\sqrt{4\pi\rho_0}} = c_1 e^{-ay} \cos(ax) \cos[Lax (e^{-ay} \cos(ax))^{-1}] \sin[(t + t_0)L\omega_0] . \qquad (3)$$

This result expresses that the induced magnetic field B_z rises from the lower boundary (i.e., $y = 0$) and spreads upward with a characteristic time scale $L\omega_0$, where L is defined by Equation (A.8). It could be noticed from Equation (3) that B_z decreases exponentially

with respect to the increase of y (height), because the term. $\cos[Lax\,(e^{-av}\cos(ax))^{-1}]$ in the central region, varies slowly with height.

Finally, the coefficient c_1 corresponds to the shear velocity (w_c). The part of the total upward Lorentz force $(-J_xB_z = -\partial/\partial y(B_z^2/2))$, that causes upward acceleration is independent of the sign of the coefficient c_1 (or w_c).

3.2. SHEAR-INDUCED INSTABILITY

From the simulation results shown in Figure 7, we found earlier that instability sets in when the absolute maximum planar velocity exceeds the Alfvén speed. In order to substantiate this claim, we performed a linearized analysis in which an approximate linearized solution for the planar velocities (u, v) was constructed as shown in the Appendix (Equation (A.13)). These velocities are as follows:

$$u_1 = \delta' e^{-2av}\sin(2ax),$$
$$v_1 = \delta' e^{-2av}[1 + \cos 2(ax)].$$
(4)

The electric current along the z-axis can be estimated, to the first order, as

$$\frac{4\pi}{c} J_z = \frac{\partial B_y}{\partial x} - \frac{\partial B_x}{\partial y} = 16a^2 B_0 e^{-3av}\cos ax \int_0^t \delta'\,dt.$$
(5)

which means that the Lorentz force $c^{-1}(J_zB_x - J_xB_z)$ leads to ascending flow, because it has been shown in the Appendix that δ' is always positive and has an exponential growth rate as shown in Equation (A.16). We have identified this phenomenon as the shear-induced instability since the numerical simulation results shown in Figure 7 are consistent with the analytical analysis. It is further noted from numerical results that the term $-c^{-1}J_xB_z$ is always upward.

The results for the evolution of the magnetic field configuration shown in Figures 2, 5, and 6 show clearly the two-stage evolution that we discussed earlier. The first stage of the evolution can be described by the linearized solution given in Equation (4). The second stage of the evolution involves the pinching together of field lines in the region where the shear motion was applied. If the three factors noted earlier (compressibility, pressure gradients, and gravity) had been absent, we believe that our results would have been similar to those of Mikic, Barnes, and Schnack (1988). Our current sheet, however, developed horizontally, whereas their current sheet was vertical. We explain this phenomenon by examining the distribution of upward component of the Lorentz force (i.e., $c^{-1}(J_zB_x - J_xB_z)$). To illustrate this viewpoint, we use the results for $\beta_0 = 0.06$ because this case best resembles the real physical conditions in active regions. The results are plotted in Figure 8. The left-most panels show the horizontal distribution of the vertical component of the Lorentz force at different heights from y_1 to y_{10} (as shown in Figure 1(b)) at 25 s after the introduction of the shear motion at the lower boundary. A noted earlier, the Alfvén time for this case is ~ 35 s. This result clearly indicates the first stage of the evolution due to the introduction of shear. All the forces are in the
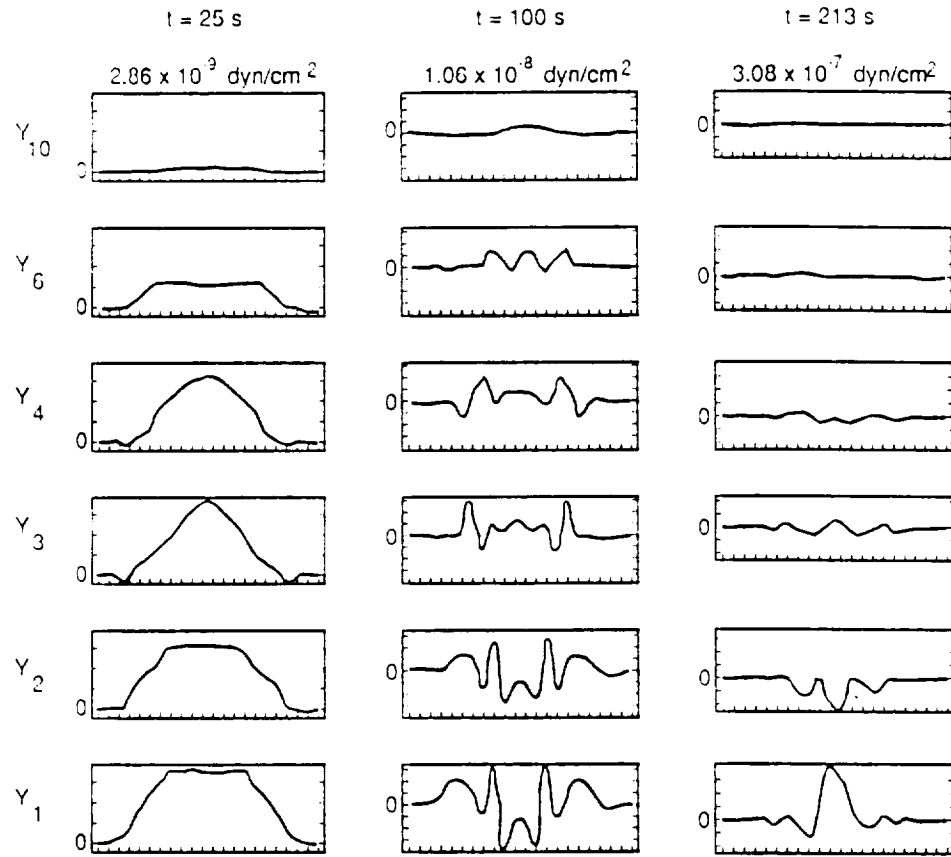
Fig. 8.   The total y-component of the Lorentz force per unit area at t = 25 s. 100 s. and 213 s and at various levels in the solar atmosphere (y = y_1, y_2, ..., etc.). The representative Alfvén time for case (iii) is 35 s and β_0 = 0.06. At t = 100 s (about $3\tau_A$) during the nonlinear stage of evolution. the Lorentz forces at the intermediate heights have a combination of upward and downward directions that causes magnetic field line pinching (see text). This pinch effect is more pronounced at t = 213 s (about $7\tau_A$) at lower altitudes. The horizontal axis represents the distance x_1 ... x_{22} as shown in Figure 1(b) also shown for Figures 2–6.

upward direction which means that all field lines are lifted up in an orderly fashion. The magnitude of these forces is of the order of 3×10^{-9} dyne cm^{-2}. The middle panels show the resultant upward component of the Lorentz force at t = 100 s which is about three Alfvén periods. These results are reflected in the nonlinear nature of the evolution in which the Lorentz forces have both upward and downward direction at the intermediate altitudes.

This bi-directional nature of the Lorentz forces causes the field lines to be pinched together in the lower regions as shown. for example. in Figure 6 for β_0 = 0.06. This particular feature is most pronounced in the results shown in the right-most panels which show the vertical component of Lorentz force at t = 213 s: this is about seven Alfvén periods after the introduction of the shear. We note that the vertical component of this Lorentz force decreases at high levels. but, in lower levels (i.e.. y_1 and y_2), two very strong oppositely-directed vertical components of Lorentz force ($\sim 3 \times 10^{-7}$ dyne cm^{-2}) appear. The force at y_1 is upward and the force at y_2 is downward.

These two forces cause the field lines to be pinched together as shown in Figure 6(c). Further discussion of this point will be included in the next section as part of a general scenario for shearing motions of magnetic arches or bipolar regions.

4. Scenario

From these simulation results. supported by the linearized analytical solution. a physical scenario is proposed for the formation of an 'Arch Filament System (AFS)' and its eruption as part of a more general scenario for 'Coronal Mass Ejections (CMEs)'. A schematic representation of this scenario is presented in Figure 9. After introduction of shear motion at a bi-polar region. all of the field lines will first be lifted up in an orderly fashion due to the shear-induced upward Lorentz force before the absolute maximum upward velocity reaches the local Alfvén speed: this is the linear stage of the evolution. When this upward velocity is in the neighbourhood of the local Alfvén speed. the lower parts of the magnetic field lines are pinched together. and an arch filament system is formed. At the same time. the upper part of the magnetic field lines is pushed upward. and a certain amount of mass is carried upward. This upward mass motion is shown in Figure 10 in terms of contours of $\Delta\rho$ and Δp that move upward at all but the lowest gravitationally-bound heights.
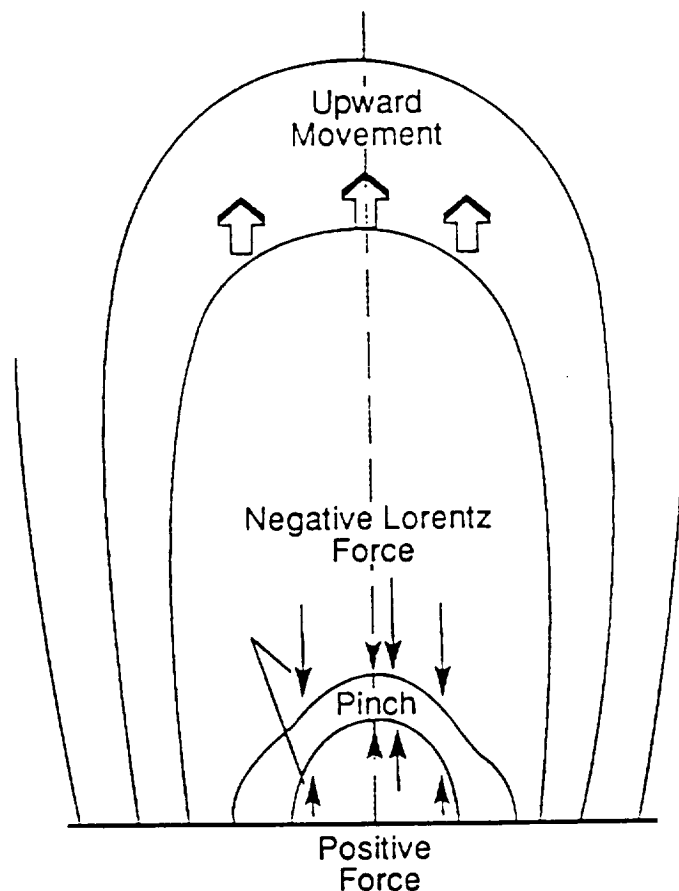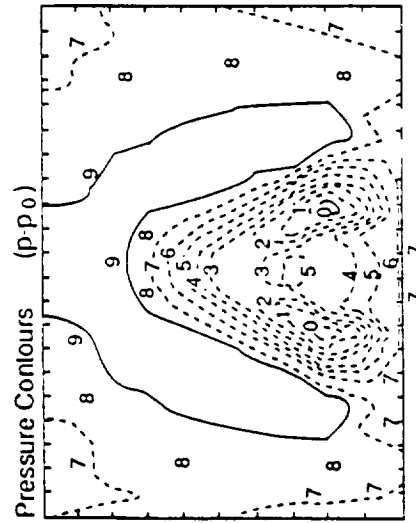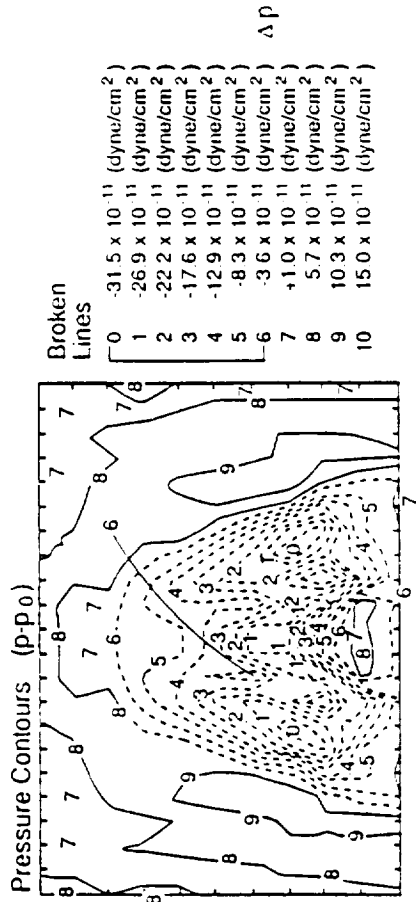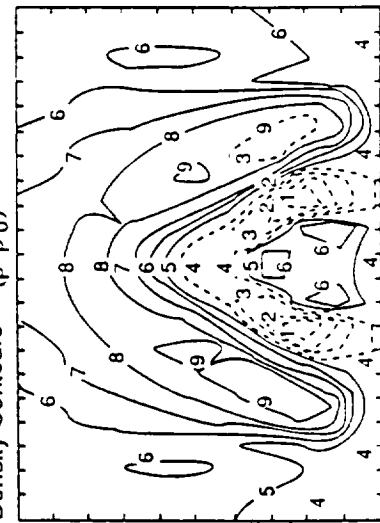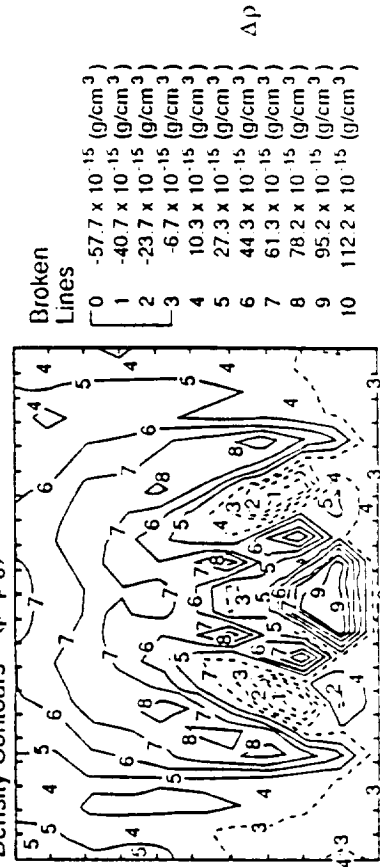

Fig. 9.   Scenario for the formation of an arch-filament system (AFS) and upper level movement outward in the initial stage of a coronal mass ejection (CME) as a result of shear-induced instability.

β₀ = 1.54

Time = 400 s

Pressure Contours (p-p₀)

Δp

Broken Lines		
0	-31.5 x 10⁻¹¹	(dyne/cm²)
1	-26.9 x 10⁻¹¹	(dyne/cm²)
2	-22.2 x 10⁻¹¹	(dyne/cm²)
3	-17.6 x 10⁻¹¹	(dyne/cm²)
4	-12.9 x 10⁻¹¹	(dyne/cm²)
5	-8.3 x 10⁻¹¹	(dyne/cm²)
6	-3.6 x 10⁻¹¹	(dyne/cm²)
7	+1.0 x 10⁻¹¹	(dyne/cm²)
8	5.7 x 10⁻¹¹	(dyne/cm²)
9	10.3 x 10⁻¹¹	(dyne/cm²)
10	15.0 x 10⁻¹¹	(dyne/cm²)

Density Contours (ρ-ρ₀)

Δρ

Broken Lines		
0	-57.7 x 10⁻¹⁵	(g/cm³)
1	-40.7 x 10⁻¹⁵	(g/cm³)
2	-23.7 x 10⁻¹⁵	(g/cm³)
3	-6.7 x 10⁻¹⁵	(g/cm³)
4	10.3 x 10⁻¹⁵	(g/cm³)
5	27.3 x 10⁻¹⁵	(g/cm³)
6	44.3 x 10⁻¹⁵	(g/cm³)
7	61.3 x 10⁻¹⁵	(g/cm³)
8	78.2 x 10⁻¹⁵	(g/cm³)
9	95.2 x 10⁻¹⁵	(g/cm³)
10	112.2 x 10⁻¹⁵	(g/cm³)

(10b)

Time = 300 s

Pressure Contours (p-p₀)

Δp

Broken Lines		
0	-28.3 x 10⁻¹¹	(dyne/cm²)
1	-24.3 x 10⁻¹¹	(dyne/cm²)
2	-20.3 x 10⁻¹¹	(dyne/cm²)
3	-16.3 x 10⁻¹¹	(dyne/cm²)
4	-12.3 x 10⁻¹¹	(dyne/cm²)
5	-8.4 x 10⁻¹¹	(dyne/cm²)
6	-4.4 x 10⁻¹¹	(dyne/cm²)
7	-0.39 x 10⁻¹¹	(dyne/cm²)
8	3.6 x 10⁻¹¹	(dyne/cm²)
9	7.6 x 10⁻¹¹	(dyne/cm²)
10	11.6 x 10⁻¹¹	(dyne/cm²)

Density Contours (ρ-ρ₀)

Δρ

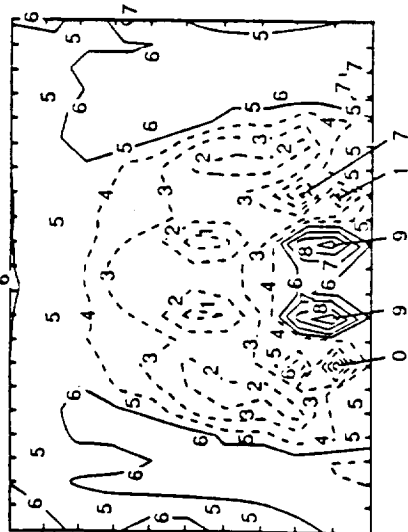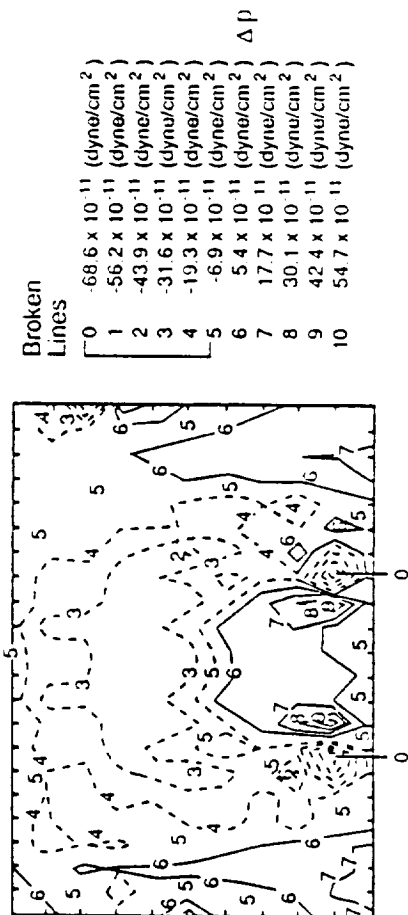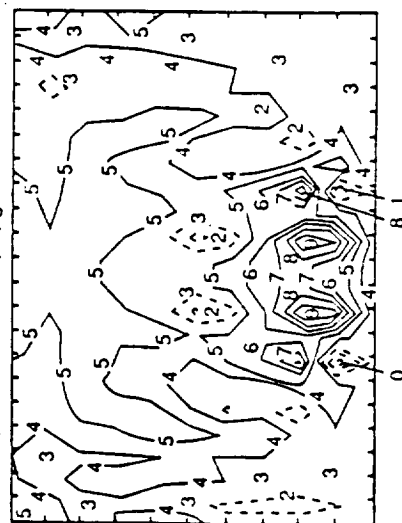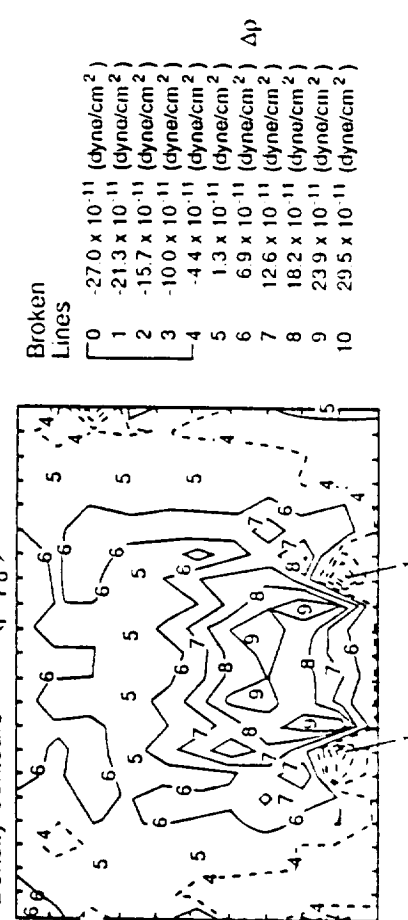| Broken Lines		
0	-57.8 x 10⁻¹⁵	(g/cm³)
1	-44.0 x 10⁻¹⁵	(g/cm³)
2	-30.1 x 10⁻¹⁵	(g/cm³)
3	-16.3 x 10⁻¹⁵	(g/cm³)
4	-2.5 x 10⁻¹⁵	(g/cm³)
5	11.3 x 10⁻¹⁵	(g/cm³)
6	25.1 x 10⁻¹⁵	(g/cm³)
7	38.9 x 10⁻¹⁵	(g/cm³)
8	52.7 x 10⁻¹⁵	(g/cm³)
9	66.5 x 10⁻¹⁵	(g/cm³)
10	80.4 x 10⁻¹⁵	(g/cm³)

(10a)

Fig. 10. Contours of pressure and density changes, $\Delta p/p_0$ and $\Delta \rho/\rho_0$, for case (ii) [$\beta_0 = 1.54$] at several times.

$\beta_o = 1.54$

Time = 600 s

Pressure Contours $(p - p_o)$

Broken Lines		Δp
0	-68.6 × 10⁻¹¹	(dyne/cm²)
1	-56.2 × 10⁻¹¹	(dyne/cm²)
2	-43.9 × 10⁻¹¹	(dyne/cm²)
3	-31.6 × 10⁻¹¹	(dyne/cm²)
4	-19.3 × 10⁻¹¹	(dyne/cm²)
5	-6.9 × 10⁻¹¹	(dyne/cm²)
6	5.4 × 10⁻¹¹	(dyne/cm²)
7	17.7 × 10⁻¹¹	(dyne/cm²)
8	30.1 × 10⁻¹¹	(dyne/cm²)
9	42.4 × 10⁻¹¹	(dyne/cm²)
10	54.7 × 10⁻¹¹	(dyne/cm²)

Density Contours $(\rho - \rho_o)$

Broken Lines		$\Delta \rho$
0	-27.0 × 10⁻¹¹	(dyne/cm²)
1	-21.3 × 10⁻¹¹	(dyne/cm²)
2	-15.7 × 10⁻¹¹	(dyne/cm²)
3	-10.0 × 10⁻¹¹	(dyne/cm²)
4	-4.4 × 10⁻¹¹	(dyne/cm²)
5	1.3 × 10⁻¹¹	(dyne/cm²)
6	6.9 × 10⁻¹¹	(dyne/cm²)
7	12.6 × 10⁻¹¹	(dyne/cm²)
8	18.2 × 10⁻¹¹	(dyne/cm²)
9	23.9 × 10⁻¹¹	(dyne/cm²)
10	29.5 × 10⁻¹¹	(dyne/cm²)

(10d)

Time = 500 s

Pressure Contours $(p - p_o)$

Broken Lines		Δp
0	-50.7 × 10⁻¹¹	(dyne/cm²)
1	-41.3 × 10⁻¹¹	(dyne/cm²)
2	-31.8 × 10⁻¹¹	(dyne/cm²)
3	-22.4 × 10⁻¹¹	(dyne/cm²)
4	-13.0 × 10⁻¹¹	(dyne/cm²)
5	-3.6 × 10⁻¹¹	(dyne/cm²)
6	5.8 × 10⁻¹¹	(dyne/cm²)
7	15.3 × 10⁻¹¹	(dyne/cm²)
8	24.7 × 10⁻¹¹	(dyne/cm²)
9	34.1 × 10⁻¹¹	(dyne/cm²)
10	43.5 × 10⁻¹¹	(dyne/cm²)

Density Contours $(\rho - \rho_o)$

Broken Lines		$\Delta \rho$
0	-11.7 × 10⁻¹⁴	(g/cm³)
1	-8.0 × 10⁻¹⁴	(g/cm³)
2	-4.2 × 10⁻¹⁴	(g/cm³)
3	-0.45 × 10⁻¹⁴	(g/cm³)
4	3.3 × 10⁻¹⁴	(g/cm³)
5	7.1 × 10⁻¹⁴	(g/cm³)
6	10.8 × 10⁻¹⁴	(g/cm³)
7	14.6 × 10⁻¹⁴	(g/cm³)
8	18.3 × 10⁻¹⁴	(g/cm³)
9	22.1 × 10⁻¹⁴	(g/cm³)
10	25.8 × 10⁻¹⁴	(g/cm³)

(10c)

Fig. 10 (continued).

Finally, when this absolute upward velocity exceeds the Alfvén speed, the shear-induced instability sets in as shown by the numerical results of Figure 7 and the analytical solution in the Appendix (Equation (A.16)). In the following we compare this scenario with the available observations.

Arch filament systems and coronal mass ejections have been investigated by many authors (Bruzek, 1967, 1968, 1969; Bumba and Howard, 1965; Martres *et al.*, 1966; Harrison, 1986). These authors have noted that arch filament systems (AFS) always connect areas of opposite polarities and cross the neutral line in the longitudinal magnetic field. Bruzek (1969) has pointed out that the occurrence of AFS is associated with evolution of young bipolar spot groups. As for the motion of AFS, its characteristic feature is its expansion in height with an ascending velocity of 16–25 km s^{-1} with footpoints rooted in the two opposite spot regions. This behaviour is quite similar to the early stage of the simulated magnetic field line evolution and mass motion shown in Figures 2, 3, 5, and 6 where the apex of the magnetic loops is rising but their legs have little lateral movement. It was further noted that the AFS has both descending and ascending motions in loops. Bruzek (1968) attributed this phenomenon to the mass injection at one leg and its return to the chromosphere via another leg that has opposite polarity. On the other hand, shearing motion, if it has a line-of-sight component, would always lead to a blue shift in one leg and red shift in the other. Therefore, observations of flows in filaments are not evidence of shearing. However, such evidence is not needed since the relative motion of bipolar spots is both necessary and sufficient evidence of shearing. Nevertheless, this concept of descending and ascending motion is based on Doppler shift measurements which can easily, at least partially, be recognized as complementary evidence of horizontal shear motion that occurs on both sides of the neutral line. This statement considers the fact that the spot group area is often not strictly perpendicular to the line of sight of the observer; thus the Doppler shift velocity must have an appreciable horizontal component (Harvey and Harvey, 1976).

On the basis of our numerical simulations, the analytial solution and observed characteristics, a physical model for the formation of AFS and subsequent CME can be constructed as follows. First, a young bipolar sunspot group emerges from the sub-photosphere. As it rises, its area increases and the neutral line dividing the opposite polarities gets longer and longer. Then a portion of the field can be reasonably regarded as a two-dimensional bipolar field (as is used in our mathematical model). In the meantime, the opposite polarity areas rotate with respect to each other. Associated with this rotation are horizontal shear motions that appear on both sides of the neutral line (thereby justifying our construction of the shearing velocity used herein). The Lorentz force generated by this process (see, for example, Figure 8) pushes the magnetic loops upward during an initial stage. At the later times, the magnetic field becomes distorted, nonlinear MHD effects force field lines to pile-up and, then, the pinch phenomenon ensues. Such pinched magnetic flux tubes could be identified as arch filaments which are visible as a set of dark loops. The simulation has shown that in this region the plasma has high density and low temperature. From the analytical solution, we notice that the growth time $(V_A a)^{-1}$ of the shearing instability is about 30 min which is a typical
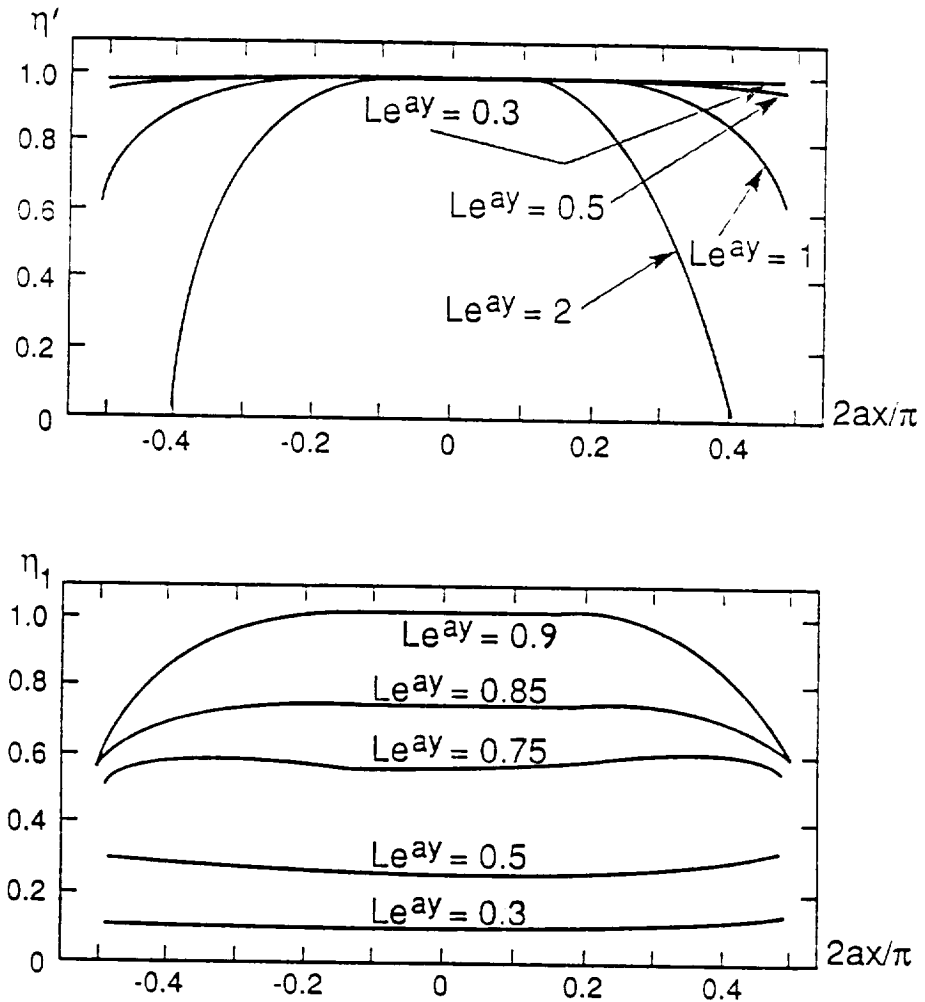
Fig. 11.   Behaviour of η' and η_1. See Appendix (Equation (A.12)).

average life time of AFS. Thus, this simulation model may be appropriate to describe the formation of AFS and the eruption which leads to some CMEs.

5. Concluding Remarks

We have used a time-dependent, nonplanar MHD model for a bipolar magnetic region that was subjected to shearing motion at its foot points. The characteristic plasma beta was varied over a wide range – from 154 to a more realistic value of 0.06. Common features were identified for all cases with the differences primarily occurring in the timing of the events vis-à-vis the characteristic Alfvén times. An essentially linear, early phase of upward mass motion was followed until the Alfvén speed was reached, and a shear-induced instability is initiated. This nonlinear instability may be the basic mechanism for arch filament formation and subsequent coronal mass ejections.

In our opinion, the early evolution in our simulation is in accord with *quasi-static* evolution of magnetic arcades demonstrated by Klimchuk and Sturrock (1989). In their work, a very low beta plasma was assumed, and therefore the magnetic field is unaffected

by pressure and gravitational forces. Our simulations are also in accord with the dynamic evolution of magnetic arcades demonstrated by the numerical simulations of Mikic, Barnes, and Schnack (1988) and Biskamp and Welter (1989) in both the *early* and *intermediate* stages of this evolution despite their neglect of compressibility, pressure gradient, and gravity. We did not find the reconnection and formation of an ejected plasmoid, as Mikic, Barnes, and Schnack (1988) did, since we assumed electrical resistivity and viscosity to be zero. During the *late* stages of the evolutionary development, when the plasma velocities surpassed the Alfvén speed, our numerical simulations demonstrate nonlinear instability and catastrophic upward motion at high altitudes.

As a final remark, it can be shown that these numerical results are valid over a wide range of parameters according to the scaling rule for dynamic similitude. For example, the present numerical results, computed on the basis of $T_0 = 10^5$ K and $\rho_0 = 1.67 \times 10^{-12}$ g cm^{-3}, can be scaled to initial conditions of $T_1 = 10^6$ K and $\rho_1 = 1.67 \times 10^{-13}$ g cm^{-3} by introducing a set of scaling parameters: $t_1 = \sqrt{\lambda}\, t_0$, $L_1 = \lambda L_0$, $v_1 = \sqrt{\lambda}\, v_0$, $T_1 = \lambda T_0$, $\rho_1 = \lambda^{-1} \rho_0$, $p_1 = p_0$, and $B_1 = B_0$ which leave the governing equations invariant for a given plasma beta. In a recent study of similitude theory, Wu *et al.* (1988) have shown that the present results also apply to the physical condition represented by these different initial conditions.

As another example of the use of dynamic similitude, we may pose the following question: if the footpoints are moved slowly enough that the evolution is quasi-static, would the magnetic field closely approximate the static equilibrium states? Although, we suggested above (as did Mikic, Barnes, and Schnack, 1988, and Biskamp and Welter, 1989) that the answer is 'yes', the reader is reminded of the values of the shearing velocity v_z used in the present studies (e.g., 15 km s^{-1}, maximum, for $\beta_0 = 0.06$) and in the above-mentioned work (30 km s^{-1}, assumed by Mikic, Barnes, and Schnack, 1988, for $\beta \sim 0.03$). Although these maximum footpoint shearing velocities are much less than the Alfvén speed, they are a factor of about 10 larger than observed photospheric velocities.

In summary, we consider the results given here to be representative of a realistic dynamical evolution of the posed physical problem of sheared magnetic arches and their evolution into arch filament eruption and coronal mass ejections.

Finally, we remark on the relevance of our results to the observations of some CMEs as reported by Harrison (1986). The major point of his work is that a small X-ray burst is often found at the very onset of a CME, often followed by a large X-ray flare later on during the CME. In the present work, the formation of the current sheet coincides with the rapid increase in the velocity of the upper portion of the field lines. One could interpret the latter, as already discussed, as the onset of CME, while the current sheet formation could lead to a burst of energy dissipation (not shown here) which would be visible as a small X-ray burst. The simultaneity of these two events is consistent with the observations of Harrison (1986). This could be another indication that these numerical results indeed represent a basic mechanism for the initiation of CMEs.

Appendix

To obtain an asymptotic solution for the relationship between the footpoint shearing velocity. w. and B_z in the first stage (linear stage) of evolution during which ρ. p. T. B_x. B_y vary slightly. we write

$$\rho = \rho_0 + \rho_1, \quad p = p_0 + p_1, \quad T = T_0 + T_1, \quad B_x = B_{x0} + B_{x1},$$

$$B_y = B_{y0} + B_{y1}, \quad B_z = B_{z1}, \quad v_x = v_{x1}, \quad v_y = v_{y1}, \quad v_z = v_{z1}. \tag{A.1}$$

where subscript 0 and 1 indicate the zero-order and first-order quantities. And. v_{x1}. v_{y1}, $|v_{z1}| \ll B_0/\sqrt{4\pi\rho_0} = $ Alfvén speed. $|B_{z1}| \ll B_0$. Inserting (A.1) into Equations (2.4) and (2.7) formerly given by Wu, Hu, and Nakagawa (1983) and leaving out the higher-order quantities. we obtain the linearized equations

$$\frac{\partial v_{z1}}{\partial t} = \frac{B_{x0}}{\sqrt{4\pi\rho_0}} \frac{\partial(B_{z1}/\sqrt{4\pi\rho_0})}{\partial x} + \frac{B_{y0}}{\sqrt{4\pi\rho_0}} \frac{\partial(B_{z1}/\sqrt{4\pi\rho_0})}{\partial y} - \frac{b}{2} \frac{B_{x0}}{\sqrt{4\pi\rho_0}} \frac{B_{z1}}{\sqrt{4\pi\rho_0}}.$$

$$\frac{\partial(B_{z1}/\sqrt{4\pi\rho_0})}{\partial t} = \frac{B_{x0}}{\sqrt{4\pi\rho_0}} \frac{\partial v_{z1}}{\partial x} + \frac{B_{y0}}{\sqrt{4\pi\rho_0}} \frac{\partial v_{z1}}{\partial y}, \tag{A.2}$$

where $\rho_0 = \rho_c e^{-by}$, $b = g/RT_c$. To solve Equation (A.2), we construct the auxiliary equations

$$\frac{\partial v_z^*}{\partial t} = B_{x0}(4\pi\rho_0)^{-1/2} \frac{\partial(B_z^*/\sqrt{4\pi\rho_0})}{\partial x} + B_{y0}(4\pi\rho_0)^{-1/2} \frac{\partial(B_z^*/\sqrt{4\pi\rho_0})}{\partial y}.$$

$$\frac{\partial(B_z^*/\sqrt{4\pi\rho_0})}{\partial t} = B_{x0}(4\pi\rho_0)^{-1/2} \frac{\partial v_z^*}{\partial x} + B_{y0}(4\pi\rho_0)^{-1/2} \frac{\partial v_z^*}{\partial y}. \tag{A.3}$$

Substituting

$$F^+ = \frac{\left(v_z^* + \dfrac{B_z^*}{\sqrt{4\pi\rho_0}}\right)}{2}, \qquad F^- = \frac{\left(v_z^* - \dfrac{B_z^*}{\sqrt{4\pi\rho_0}}\right)}{2},$$

Equations (A.3) reduce to

$$\frac{\partial F^+}{\partial t} = B_0(4\pi\rho_c)^{-1/2} e^{-(a-b/2)v}\left(\cos ax\,\frac{\partial F^+}{\partial x} - \sin ax\,\frac{\partial F^+}{\partial y}\right),$$

$$\frac{\partial F^-}{\partial t} = B_0(4\pi\rho_c)^{-1/2} e^{-(a-b/2)v}\left(-\cos ax\,\frac{\partial F^-}{\partial x} + \sin ax\,\frac{\partial F^-}{\partial y}\right).$$ (A.4)

Since solving Equations (A.4) is equivalent to solving their corresponding ordinary differential equations (Courant and Hilbert, 1962), it is easy to write down the solutions as follows:

$$F^+ = \phi(e^{-av}\cos ax,\, t\omega_0 + f(ax)(e^{-av}\cos ax)^{-1+b(2a)^{-1}}),$$

$$F^- = \psi(e^{-av}\cos ax,\, t\omega_0 - f(ax)(e^{-av}\cos ax)^{-1+b(2a)^{-1}}).$$ (A.5)

where

$$\omega_0 = aB_0(4\pi\rho_c)^{-1/2},\qquad f(x) \equiv \int_0^x (\cos x')^{-b/2a}\,\mathrm{d}x'\,.$$

Considering the boundary value of v_z (the nature of shearing) and using Equation (A.5) we can find the following solutions:

$$v_z^* = c_1 e^{-av}\cos ax\,\cos(L\zeta)\sin(L\eta),$$ (A.6)

$$\left(\frac{B_z^*}{\sqrt{4\pi\rho_0}}\right) = c_1 e^{-av}\cos ax\,\sin(L\zeta)\cos(L\eta),$$

where

$$\zeta \equiv (t + t_0)\omega_0,\qquad \eta \equiv f(ax)(e^{-av}\cos ax)^{-1+b(2a)^{-1}}.$$

t_0, L, and c_1 are integration constants. Back to solving Equations (A.2) suppose v_{z1}, $(B_z/\sqrt{4\pi\rho_0})$ satisfy the equalities (A.6) except that L, c_1 are now not constants but functions of x, y. Thus

$$v_{z1} = c_1(x, y)\,e^{-av}\cos(ax)\cos(L(x, y)\zeta)\sin(L(x, y)\eta),$$ (A.7)

$$\left(\frac{B_{z1}}{\sqrt{4\pi\rho_0}}\right) = c_1(x, y)\,e^{-av}\cos(ax)\sin(L(x, y)\zeta)\cos(L(x, y)\eta).$$

Inserting (A.7) into (A.2), c_1 and L can be determined uniquely by solving two ordinary differential equations. First, L satisfies the equation

$$\cos ax\,\frac{\partial L}{\partial x} - \sin ax\,\frac{\partial L}{\partial y} = Q(x, y, L),$$

$$Q(x, y, L) \equiv -(b/4)\sin(ax)\sin(2L\zeta)\sin(2L\eta) \times$$ (A.8)

$$\times\,[\zeta\sin(2L\eta) - \eta\sin(2L\zeta)]^{-1},$$

with boundary condition $L|_{y=0} = L(x)$. After L has been found. $(\ln c_1)$ can be obtained in the same manner using the following equation:

$$\cos(ax)\,\frac{\partial(\ln c_1)}{\partial x} - \sin(ax)\,\frac{\partial(\ln c_1)}{\partial y} = [\zeta\,\mathrm{tg}(L\zeta) - \eta\,\mathrm{ctg}(L\eta)]\,Q(x,y,L).$$

(A.9)

In fact. we only apply (A.7) to explain the physical nature in the lower shearing region where $\bar{\rho}_0 \simeq 0.8\rho_c$, therefore L and c_1 can roughly be regarded as constants.

It is difficult to find an asymptotic solution for v_x and v_y. Let us consider case (iii) of strong magnetic field. in which the inertial force and $-\nabla p$ and ρg can safely be ignored. Inserting (A.1) into (2.2) and (2.3) of Wu. Hu. and Nakagawa (1983). the linearized equations are given as follows:

$$\bar{\rho}_0\,\frac{\partial v_{x1}}{\partial t} = \frac{1}{4\pi}\,B_{y0}\left(\frac{\partial B_{x1}}{\partial y} - \frac{\partial B_{y1}}{\partial x}\right) - \frac{1}{4\pi}\,B_{z1}\,\frac{\partial B_{z1}}{\partial x}.$$

$$\bar{\rho}_0\,\frac{\partial v_{y1}}{\partial t} = -\frac{1}{4\pi}\,B_{x0}\left(\frac{\partial B_{x1}}{\partial y} - \frac{\partial B_{y1}}{\partial x}\right) - \frac{1}{4\pi}\,B_{z1}\,\frac{\partial B_{z1}}{\partial y}.$$

(A.10)

where the terms

$$-\frac{1}{4\pi}\,B_{z1}\,\frac{\partial B_{z1}}{\partial x}, \qquad -\frac{1}{4\pi}\,B_{z1}\,\frac{\partial B_{z1}}{\partial y},$$

which are second-order quantities. must be kept in view of actual mathematical manipulation. From (A.7) the partial Lorentz force can be written as

$$-(4\pi\bar{\rho}_0)^{-1}B_{z1}\,\frac{\partial B_{z1}}{\partial x} = (c_1^2 a/2)\,(\eta' + \eta_1)\,e^{-2ay}\sin(2ax)\sin^2(L\zeta),$$

(A.11)

$$-(4\pi\bar{\rho}_0)^{-1}B_{z1}\,\frac{\partial B_{z1}}{\partial y} = (c_1^2 a/2)\eta'\,e^{-2ay}[1 + \cos(2ax)]\sin^2(L\zeta),$$

where η' and η_1 are slow-varying functions of x, y. The representations for η'. η_1 are very complicated in the case with gravity, but we only deal with the lower central part of the domain where $\rho \simeq$ const. Thus, the gravitational effects could be ignored in Equation (A.2). then leading to the solution. $\eta \simeq ax\,e^{ay}(\cos ax)^{-1}$, $B_{z1} \simeq B_z^*$. Therefore. η' and η_1 asymptotically approach the case with no gravity. In such case η' and η_1 take simple forms as

$$\eta' = (\cos\Pi)^2 + \Pi\cos\Pi\sin\Pi,$$

$$\eta_1 = L\,e^{ay}\cos\Pi\sin\Pi\,(\sin ax)^{-1},$$

(A.12)

$$\Pi = L\,e^{ay}ax\,(\cos ax)^{-1}.$$

Figure 11 shows the behaviour of η' and η_1. Note that if $L\,e^{av}$ is less than 0.5, then $0 < \eta_1 \ll \eta' \simeq 1$. Therefore we will pay no attention to the difference between η and $\eta' + \eta_1$ within the range $ax < \pi/4$. (A.11) reminds us of analogy between shearing velocity and force, so we suppose velocity having a mushroom-like form as

$$v_{x1} = \delta'\,e^{-2av}\sin ax, \qquad v_{y1} = \delta'\,e^{-2av}[1 + \cos(2ax)]. \tag{A.13}$$

where δ' is a function of t, x, y (but weakly depends on x, y) being determined later. Inserting (A.13) into the linearized equations of (2.5) and (2.6), of Wu et al. (1983) the time variation of current J_{z1}/c can be found as

$$\frac{\partial}{\partial t}\left(\frac{\partial B_{y1}}{\partial x} - \frac{\partial B_{x1}}{\partial y}\right) = 16a^2 B_0 \delta'\,e^{-3av}\cos(ax). \tag{A.14}$$

In deriving Equation (A.14) the weak dependence of δ' on x, y has been used. Differentiating (A.10) with respect to t and inserting (A.14) and (A.11) into it and then letting it go to limitation when y goes to zero, we obtain one equation

$$\frac{\partial^2}{\partial t^2}\delta'\Big|_{y=0} = 8v_A^2 a^2 \delta'\Big|_{y=0} + (c_1^2 a/2)\eta'\Big|_{y=0}L\omega_0 \sin[2L\omega_0(t + t_0)] \tag{A.15}$$

to determine δ' uniquely (here $v_A^2 = B_0^2/4\pi\bar{\rho}_0$). Noticing δ', η' only weakly depend on x, y, Equation (A.15) can be regarded as an ordinary differential equation and, therefore, can be easily integrated with respect to t. Giving the initial condition: $\delta'|_{y=0} = 0$, $d\delta'/dt|_{y=0} = 0$ when $t = 0$, we obtain an asymptotic solution as

$$\delta'|_{y=0} = [(\alpha + \beta)/2]\exp(\sqrt{8}\,v_A at) + [(\alpha - \beta)/2]\exp(-\sqrt{8}\,v_A at) -$$
$$- \alpha\,\frac{\sin[2L\omega_0(t + t_0)]}{\sin[2L\omega_0 t_0]}. \tag{A.16}$$

with

$$\alpha = \frac{L\omega_0 ac_1^2\eta'|_{y=0}}{8(L^2\omega_0^2 + 2v_A^2 a^2)}\sin(2L\omega_0 t_0) \sim \frac{L\eta' c_1^2/v_A}{8\sqrt{2}(L^2 + 2)} > 0.$$

$$\beta = \frac{L^2\omega_0^2 c_1^2\eta'|_{y=0}}{8\sqrt{2}\,v_A(L^2\omega_0^2 + 2v_A^2 a^2)}\cos(2L\omega_0 t_0) \sim \frac{L^2\eta' c_1^2/v_A}{16(L^2 + 2)} > 0.$$

Generally, we can find an approximate solution for the average $\bar{\delta}'$, the representation of which is the same as (A.16) except for the substitutions $\delta'|_{y=0}, \eta'|_{y=0}, v_A^2$ by $\bar{\delta}', \bar{\eta}', \bar{v}_A^2$, where

$$\bar{\delta}' = \int_0^{y_2}\delta'\,dy/y_2, \qquad \bar{\eta}' = \int_0^{y_2}\eta'\,dy/y_2, \qquad \bar{v}_A^2 = V_A^2\int_0^{y_2}e^{-2av}\,dy/y_2.$$

From (A.16) it can be seen that δ will grow exponentially. and that the shearing velocity c_1 acts like a 'seed'. If there is no 'seed'. the mushroom flow velocities (v_x, v_y) will never arise. The growth rate is independent of c_1 but depends on the Alfvén speed $v_A = B_0 / \sqrt{4\pi\rho_0}$. Therefore. shear motion can induce linear MHD-instability. However. this instability soon attains saturation. and the flow becomes quasi-steady and increases gradually until the velocities (v_x, v_y) exceed v_A.

References

Biskamp. D. and Welter. H.: 1989. *Solar Phys.* **120**. 49.

Bruzek. A.: 1967. *Solar Phys.* **2**. 451.

Bruzek. A.: 1968. in K. O. Kiepenheuer (ed.). 'Structure and Development of Solar Active Region'. *IAU Symp.* **35**. 293.

Bruzek. A.: 1969. *Solar Phys.* **8**. 29.

Bumba. V. and Howard. R.: 1965. *Astrophys. J.* **141**. 1492.

Courant. R. and Hilbert. D.: 1962. *Methods of Mathematical Physics*. Interscience Publ.. New York.

Gold. T. and Hoyle. F.: 1960. *Monthly Notices Roy. Astron. Soc.* **120**. 89.

Hagyard. M. J.: 1991. *Mem. Soc. Astron. Ital.* (in press).

Harrison. R.: 1986. *Astron. Astrophys.* **162**. 283.

Harvey. J. W. and Harvey. K. L.: 1976. *Solar Phys.* **47**. 233.

Hu. Y. Q. and Wu. S. T.: 1984. *J. Comp. Phys.* **55**. 33.

Klimchuk. J. A. and Sturrock. P. A.: 1989. *Astrophys. J.* **345**. 1034.

Klimchuk. J. A.. Sturrock. P. A.. and Yang. W.-H.: 1988. *Astrophys. J.* **335**. 456.

Krall. K. R. *et al.*: 1982. *Solar Phys.* **79**. 59.

Low. B. C.: 1977, *Astrophys. J.* **212**. 234.

Low. B. C.: 1981, *Astrophys. J.* **251**. 352.

Low. B. C. and Nakagawa. Y.: 1975. *Astrophys. J.* **199**. 237.

Martres. M. J. *et al.*: 1966. *Ann. Rev. Astron. Astrophys.* **29**. 245.

Mikic. D. Z.. Barnes. D. C.. and Schnack. D. D.: 1988. *Astrophys. J.* **328**. 830.

Nakagawa. Y.. Hu. Y. Q.. and Wu. S. T.: 1987. *Astron. Astrophys.* **179**. 354.

Švestka. Z.: 1976. *Solar Flares*. D. Reidel Publ. Co.. Dordrecht. Holland.

Tanaka. K. and Nakagawa. Y.: 1973. *Solar Phys.* **33**. 187.

Wu. S. T. and Wang. J. F.: 1987. *Comp. Methods Applied Mech. Eng.* **64**. 267.

Wu. S. T.. Hu. Y. Q.. and Nakagawa. Y.: 1983. *Astrophys. J.* **266**. 866.

Wu. S. T.. Hu. Y. Q.. and Krall. K. R.: 1984. *Solar Phys.* **90**. 117.

Wu. S. T.. Hu. Y. Q.. Nakagawa. Y.. and Tandberg-Hanssen. E.: 1986. *Astrophys. J.* **306**. 751.

Wu. S. T.. Wang. S.. Wang. A. H.. and Dryer. M.: 1988. *Adv. Space Sci.* **8**(11). 221.